Dynamics of the geomagnetically disturbed ionosphere as measured by GPS receivers and SuperDARN HF radars

Evan Grier Thomas

Thesis submitted to the faculty of the Virginia Polytechnic Institute and State University
in partial fulfillment of the requirements for the degree of

Master of Science
in
Electrical Engineering

J. Michael Ruohoniemi, Co-Chair
Joseph B. H. Baker, Co-Chair
Timothy Pratt
Wayne A. Scales

11/28/2012
Blacksburg, Virginia

Keywords: SuperDARN, GPS, mid-latitude, ionosphere

Dynamics of the geomagnetically disturbed ionosphere as measured by GPS receivers and SuperDARN HF radars

Evan Grier Thomas

ABSTRACT

Total electron content (TEC) data measured from ground-based GPS receivers is compared to HF backscatter from ionospheric irregularities obtained by Super Dual Auroral Radar Network (SuperDARN) radars. We present the first observations of a recurrent region of anomalous enhanced TEC at mid-latitudes over North America and attempt to characterize its frequency of occurrence. Next, we examine the relationship of convection electric fields to the formation of a polar cap tongue of ionization (TOI) from mid-latitude plumes of storm enhanced density (SED) during a geomagnetic storm on 26 September 2011. A channel of high density F region plasma was transported from the dayside ionosphere and into the polar cap by enhanced convection electric fields extending to mid-latitudes. After the solar wind IMF conditions quieted and the dayside convection electric fields retreated to higher latitudes, an SED was observed extending to, but not entering, the dayside cusp region. The source mechanism (enhanced electric fields) previously drawing the plasma from mid-latitudes and into the polar cap was no longer active, resulting in a fossil feature which persisted for several hours as it elongated in magnetic local time. Finally, we discuss ground surface effects on the HF backscatter observed by four SuperDARN radars. Monthly ground scatter occurrence rates are calculated for comparison with Arctic sea ice boundaries derived from satellite observations, showing reduced backscatter from regions covered by ice.

Acknowledgments

I would like to start by thanking my advisors, Dr. Jo Baker and Dr. Mike Ruohoniemi, for all of their guidance and support over the last several years as a member of their research group. Thank you to Dr. Lasse Clausen for always showing great patience when answering my programming questions. A special thanks also goes to all of my labmates for their support in the lab, at radar sites, and at meetings.

I would like to thank Drs. Anthea Coster, John Foster, and Phil Erickson at MIT Haystack Observatory for their valuable feedback and advice as co-authors on my first peer-reviewed journal submission. I would also like to thank Bill Rideout for his assistance in accessing and downloading GPS total electron content data from the Madrigal database.

Finally, I would like to thank my family for their love and support in helping me become the person I am today. And a very special thanks to Rachel for putting up with all of the time that went into this thesis.

Contents

1 Introduction **1**

1.1 The Ionosphere 1

1.2 SuperDARN 6

1.3 Global Positioning System 10

1.4 Thesis Organization 12

2 GPS Total Electron Content **13**

2.1 Introduction 13

2.2 Online Plotting Tools 18

2.3 Seasonal Variations and a North American Anomaly 21

2.4 Summary 27

3 Direct observations of the role of convection electric field in the formation of a polar tongue of ionization from storm enhanced density **28**

Abstract 28

3.1 Introduction 29

3.2 Datasets 30

3.2.1 SuperDARN HF Radars 30

3.2.2 GPS Total Electron Content 33

3.2.3 Online Plotting Tools 36

3.3 Observations 36

3.3.1 Event Overview 36

3.3.2 Formation of TOI 38

3.3.3 Storm Enhanced Density 41

3.4 Discussion 44
3.5 Summary 47
Acknowledgments 48

4 Active remote sensing of sea ice cover using SuperDARN HF radars 49
4.1 Introduction 49
4.2 Methodology 54
4.3 Results 55
4.3.1 Goose Bay 57
4.3.2 Stokkseyri 58
4.3.3 Saskatoon 59
4.3.4 Kapuskasing 60
4.4 Summary 61
Acknowledgments 62

5 Conclusions/Future Work 63

References 65

List of Figures

1.1 Density and composition of the daytime ionosphere and neutral atmosphere in terms of number density versus altitude based on mass-spectrometer measurements [*Luhmann*, 1995]. 2

1.2 Flow of plasma within the magnetosphere driven by magnetic reconnection. Numbered field lines show successive configurations of a magnetic field line as it undergoes reconnection. The inset shows the footpoint of the numbered field lines in the northern high-latitude ionosphere and the corresponding plasma convection pattern [*Hughes*, 1995]. 3

1.3 Propagation of HF radio waves during daytime (top) and nighttime (bottom) conditions using the 2011 International Reference Ionosphere (IRI-2011) model. Gray lines represent transmitted ray paths, pink lines are geomagnetic field lines, white lines are regularly spaced slant range intervals, and black markers are regions of backscatter from either field-aligned plasma irregularities or the Earth's surface. 5

1.4 Fields of view of currently operational SuperDARN radars in northern (left) and southern (right) hemispheres. Mid-latitude, high-latitude, and polar radar FOVs are shaded red, blue, and green respectively. 7

1.5 Modernization of GPS signals. "Present Signal" refers to the signal structure at the time of the constellation's completion in 1995 [*Coster*, 2011]. 11

2.1 Diagram showing propagation delays introduced on GPS signals by the Earth's ionosphere. 14

2.2 Comparison of GPS TEC plots on VT SuperDARN (top) and Madrigal (bottom) websites for the period around 18:10 UT on August 4th 2010. Significant differences are the longer time integration, larger spatial averaging, and logarithmic color scale used in the Madrigal plot. 17

2.3 Diagram of the median filtering grid with cell weights identified. Highlighted cell is the latitude/longitude bin currently being checked against the user-defined threshold value. 18

2.4 Examples of different median filtering threshold values and their comparison to the original GPS TEC data as downloaded from Madrigal. Figures are plotted in geomagnetic coordinates. 19

2.5 Output from the GPS/TEC Plotting - Four Plot page on the VT SuperDARN website for a SAPS event on April 9, 2011. 20

2.6 Seasonal variations in average GPS TEC over North America during geomagnetically quiet conditions (Kp $<$ 2.0) for March, June, September, and December 2008. Columns correspond to Kansas local midnight (07:00 UT, left) and noon (19:00 UT, right). 22

2.7 Diagram of geomagnetic declination and the effect of an eastward zonal wind on longitudinal variations in electron density. Magnetic field lines are into the sheet plane with dip angles I, and the sheet plane is the horizontal plan stretching into east and west, and north and south. Center vertical line represents the longitudes with zero magnetic declination. Magnetic field lines have declination D, which is positive (eastward) on the west side of the zero declination, and is negative (westward) on the east side [*Zhang et al.*, 2012]. 23

2.8 GPS TEC anomaly observed over North America at mid-latitudes on March 23rd, 2008 at 14:00 UT. The boxed region shows the latitudinal and longitudinal extent considered by the automated anomaly search function. 24

2.9 Results from automated search routine for North American anomaly for all days of year 2008. Median percent differences above +6% correspond to anomaly occurrence within the bounded search region. 26

2.10 Results from automated search routine for North American anomaly for all days of year 2009. Median percent differences above +6% correspond to anomaly occurrence within the bounded search region. 26

3.1 Fields of view of SuperDARN radars in northern (left) and southern (right) hemispheres as of July 2012. Mid-latitude, high-latitude, and polar radar FOVs are shaded red, blue, and green respectively. 32

3.2 Map of plasma convection obtained for 26 September 2011, 19:30 - 19:32 UT, using the standard SuperDARN fitting technique as described in the text and plotted in magnetic local time versus magnetic latitude with magnetic noon at the top. The contours indicate lines of constant electrostatic potential; the contour step is 6 kV and solid/dashed contours indicate negative/positive signs on the potential. The positions and 3-letter names of the radars contributing to the solution are indicated. 33

3.3 (a) Three 5-minute maps of GPS TEC observations overlaid on top of one another from 19:25-19:40 UT, after mapping to MLT-MLAT coordinates. (b) Median-filtered GPS TEC data spanning the same interval, centered at 19:30 UT. No TEC data are plotted above $\Lambda = 85°$ due to difficulties in spatial filtering over the polar cap. Figures are plotted with magnetic noon at the top and midnight at the bottom. 34

3.4 (a) GPS TEC map with SuperDARN convectin pattern overlaid and (b) line-of-sight (LOS) velocity measurements from selected SuperDARN radars with fields of view indicated, again plotted with magnetic noon at the top. 35

3.5 Geomagnetic and solar wind OMNI parameters on 26-27 September 2011 (from top): Sym-H index, OMNI IMF Bx, By, Bz, and dynamic pressure. The first shaded region indicates the interval from 18:30-19:40 UT when a TOI formed from mid-latitude SED as identified from GPS TEC maps (SED/TOI). The second shaded region indicates a later period from 20:30-00:30 UT when no TOI was observed forming from mid-latitude SED (SED/NO TOI). . . . 37

3.6 GPS TEC maps showing the development of an SED plume over North America at (a) 17:30 UT and (b) 18:00 UT on 26 September 2011. The color scale has been increased from Figure 3.3 and Figure 3.4 to highlight the region of enhanced TEC corresponding to the SED plume in (b). Figures are plotted with magnetic noon at the top. 39

3.7 (a-d) GPS TEC maps depicting evolution of a polar tongue of ionization (TOI) with SuperDARN convection patterns overlaid. (e-h) SuperDARN LOS velocity measurements from ionospheric scatter for selected radars. Figures are plotted in magnetic local time with magnetic noon at the top for times 18:00, 18:30, 19:30, and 20:00 UT. 40

3.8 In the same format as Figure 3.7, (a-d) GPS TEC maps depicting evolution of "fossil" storm enhanced density (SED), and (e-h) radar velocity measurements for times 20:30, 21:30, 22:30, and 23:30 UT. 42

3.9 Field of view of Inuvik radar with beam 5 highlighted, plotted with magnetic noon at the top of the figure for 19:30 UT. This beam looks into the polar cap and is aligned with the throat of the TOI feature described in the text. . 43

3.10 (a) The backscattered power and (b) LOS Doppler velocity data from beam 5 of the polar Inuvik radar in range-time-intensity (RTI) format. (c) GPS TEC data closest to each range cell along the same beam. In the same manner as Figure 3.5, the two intervals of SED activity as observed from GPS TEC maps are shaded. 45

4.1 Ray-tracing results for predicted ground scatter for Goose Bay radar at 15:00 UT on October 15, 2000. The 2011 International Reference Ionosphere (IRI-2011) model is used to simulate ionospheric parameters. 50

4.2 Daily average ground scatter observed by the Pykkvibaer radar in the region of Odden ice tongue. Solid lines represent approximate position of the 30% and 60% sea ice concentration boundaries determined from DMSP satellite imagery [*Shand et al.*, 1998]. 52

4.3 Seasonal variation in Rankin Inlet ground scatter occurrence and sea ice cover (gray shading) for March, June, September, and December 2008 [*Ponomarenko et al.*, 2010]. 53

4.4 Field of view/scan plot of Goose Bay ground scatter power measurements for a single scan on October 15, 2000 at 15:00 UT. 54

4.5 Monthly ground scatter occurrence rates for Goose Bay radar, averaged over 14:00-20:00 UT for the year 2000. Extent of sea ice cover at end of each month is denoted by shaded regions. 57

4.6 Monthly ground scatter occurrence rates for Stokkseyri radar, averaged over 14:00-20:00 UT for the year 2000. Extent of sea ice cover at end of each month is denoted by shaded regions. 58

4.7 Monthly ground scatter occurrence rates for Saskatoon radar, averaged over 16:00-22:00 UT for the year 2000. Extent of sea ice cover at end of each month is denoted by shaded regions. 59

4.8 Monthly ground scatter occurrence rates for Kapuskasing radar, averaged over 16:00-22:00 UT for the year 2000. Extent of sea ice cover at end of each month is denoted by shaded regions. 60

4.9 Sea surface scattering mechanism for (a) rough sea and (b) smooth sea [*Shand et al.*, 1998]. 61

List of Tables

1.1 List of current SuperDARN radars in the Northern Hemisphere. 9
1.2 List of current SuperDARN radars in the Southern Hemisphere. 9

Chapter 1

Introduction

1.1 The Ionosphere

The ionosphere is a region of weakly ionized plasma which stretches from about 50 km to 1,000 km above the Earth's surface. Although neutral components still dominate at these altitudes, the ionization is sufficient to endow the atmosphere with electrical properties. The ionosphere is divided into three principal layers: the D region (below 90 km), E region (between 90 km and 130 km), and F region (above 130 km). Oftentimes the F region is further divided into F_1 and F_2 layers because of the smaller peak sometimes seen in the density profile below the main (F_2) peak. Absorption of solar radiation by neutral molecules is the primary source of atmospheric ionization except at auroral latitudes where energetic particle precipitation can be significant. Field-aligned currents connecting the magnetosphere to the ionosphere are the primary mechanism by which these energetic particles are transported to the ionosphere. Figure 1.1 shows the density and composition of the daytime ionosphere (solid lines) and neutral atmosphere (dashed lines) in terms of number density versus altitude. The primary atmospheric layers are defined by density peaks that result from an interplay of local production, loss, and transport processes [*Luhmann*, 1995].

Conditions in the high-latitude ionosphere are largely driven by interactions between the constantly streaming plasma from the sun, called the solar wind, and the Earth's magnetic field. The solar wind is a collisionless plasma with a "frozen-in" magnetic field called the

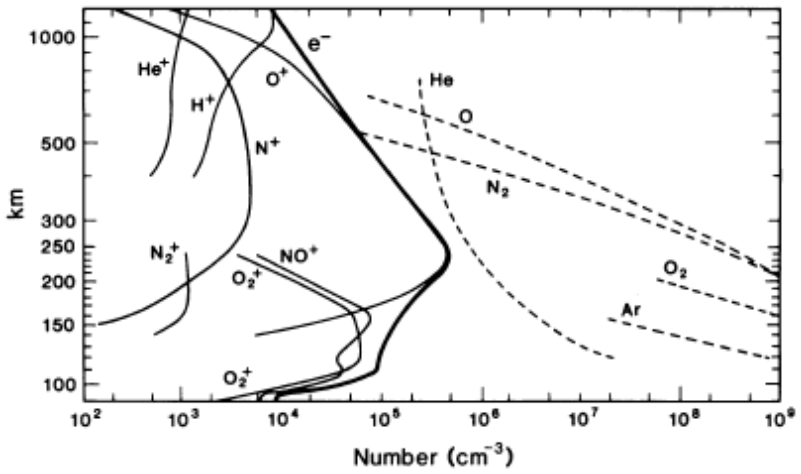

Figure 1.1: Density and composition of the daytime ionosphere and neutral atmosphere in terms of number density versus altitude based on mass-spectrometer measurements [*Luhmann*, 1995].

Interplanetary Magnetic Field (IMF). A feature called the bow shock forms about 14 Earth radii (R_E) upstream from the Earth to slow the solar wind to subsonic speeds so that it can flow around the magnetosphere. The position of the bow shock relative to the Earth depends on the pressure balance between the upstream solar wind and the region of subsonic flow behind the shock, known as the magnetosheath. Where the solar wind encounters the outer boundary of the magnetosphere, called the magnetopause, currents are generated which confine the geomagnetic field to the region interior to the magnetopause.

The solar wind compresses the magnetospheric cavity on the dayside and creates an elongated geomagnetic tail on the nightside. A current sheet lies within a region of hot plasma in the center of the geomagnetic tail, separating two tail lobes which magnetically connect to the northern and southern polar regions in the ionosphere. Magnetic reconnection occurs when a southward-oriented IMF encounters closed magnetic field lines at the front of the magnetosphere (field lines 1 and 1' in Figure 1.2). These new solar-terrestrial field lines are oriented such that one end remains attached at the Earth's pole while the other stretches out into interplanetary space, allowing particles of solar origin to move freely down

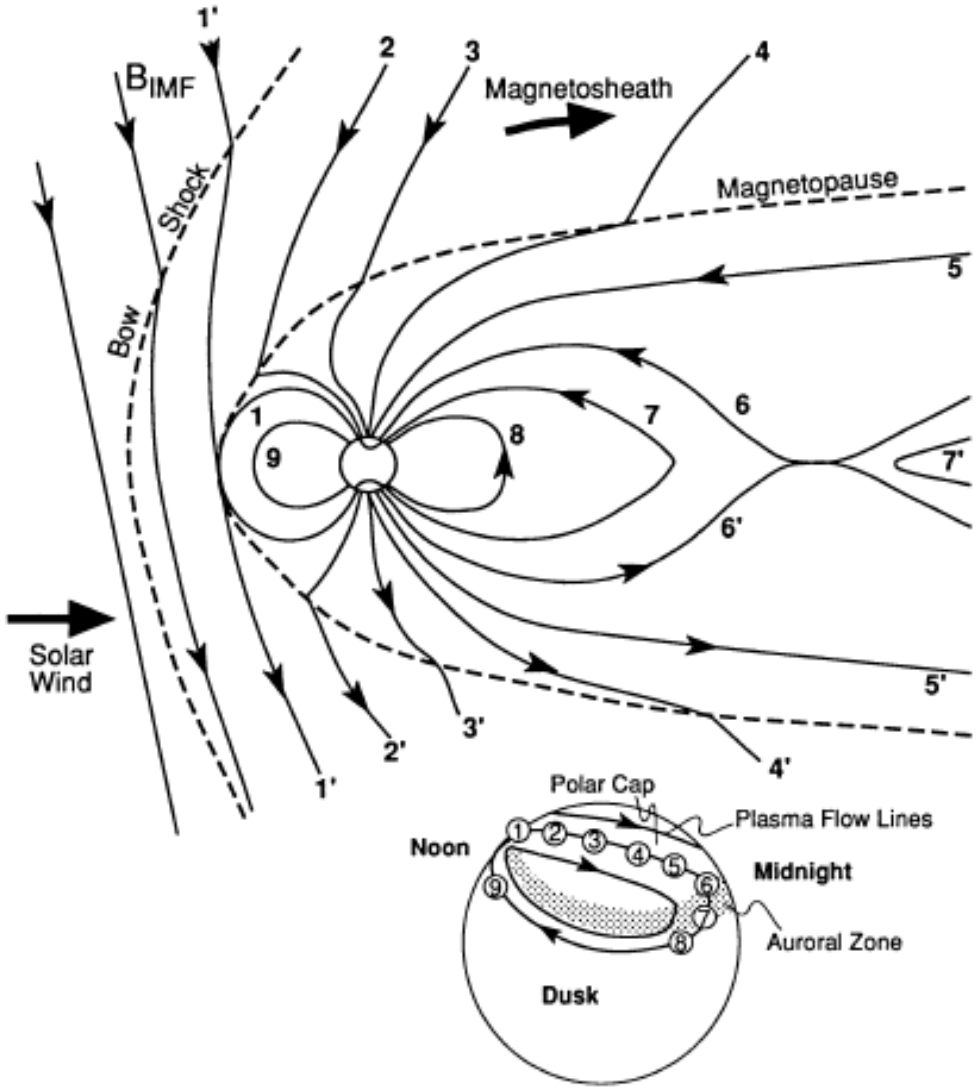

Figure 1.2: Flow of plasma within the magnetosphere driven by magnetic reconnection. Numbered field lines show successive configurations of a magnetic field line as it undergoes reconnection. The inset shows the footpoint of the numbered field lines in the northern high-latitude ionosphere and the corresponding plasma convection pattern [*Hughes*, 1995].

the highly conductive magnetic field lines into the ionosphere. As the solar wind continues to flow past the magnetosphere, the field lines move through the successive numbered locations in Figure 1.2 as they stretch out into the geomagnetic tail before finally snapping and reconnecting at positions 6 and 6'. The inset in Figure 1.2 shows the progression of the ionospheric footpoints of the numbered field lines in the northern high-latitude ionosphere as they move antisunward across the polar cap and return back to the dayside at lower latitudes [*Hughes*, 1995]. The precipitation of electrons and ions into the ionosphere along field lines can seed the formation of irregular density structures, or plasma irregularities, in the auroral ionosphere.

Ionospheric irregularities are fluctuations in electron density that have been amplified above the background level by a plasma instability [*Fejer and Kelley*, 1980; *Keskinen and Ossakow*, 1983; *Tsunoda*, 1988]. These irregularities can occupy a wide range of spatial scales, from a few centimeters to hundreds of kilometers. At F region altitudes the horizontal drift of the plasma density irregularities is dominated by the motion of the background plasma, which is related to the ionospheric electric field, $\mathbf{E}$, by

$$\mathbf{v} = \frac{\mathbf{E} \times \mathbf{B}}{B^2}$$

where $\mathbf{B}$ is the geomagnetic field. Radio waves can be reflected when propagating quasi-perpendicular to these plasma irregularities as determined by the coherent Bragg scattering condition $\mathbf{k}$ equal to $\pm 2\mathbf{k_r}$, where $\mathbf{k}$ is the wavevector of of the irregularity and $\mathbf{k_r}$ is the wavevector of the transmitted signal. Because the phase front of irregularities are aligned with geomagnetic field lines ($\mathbf{k} \perp \mathbf{B}$), backscatter occurs when the $\mathbf{k_r}$ vector of the radio wave lies in the plane perpendicular to the geomagnetic field. At high latitudes where field lines are vertical, it is nearly impossible for Very High Frequency (VHF, 30-300 MHz) and Ultra High Frequency (UHF, 300-3000 MHz) radio waves to achieve orthogonality to irregularities

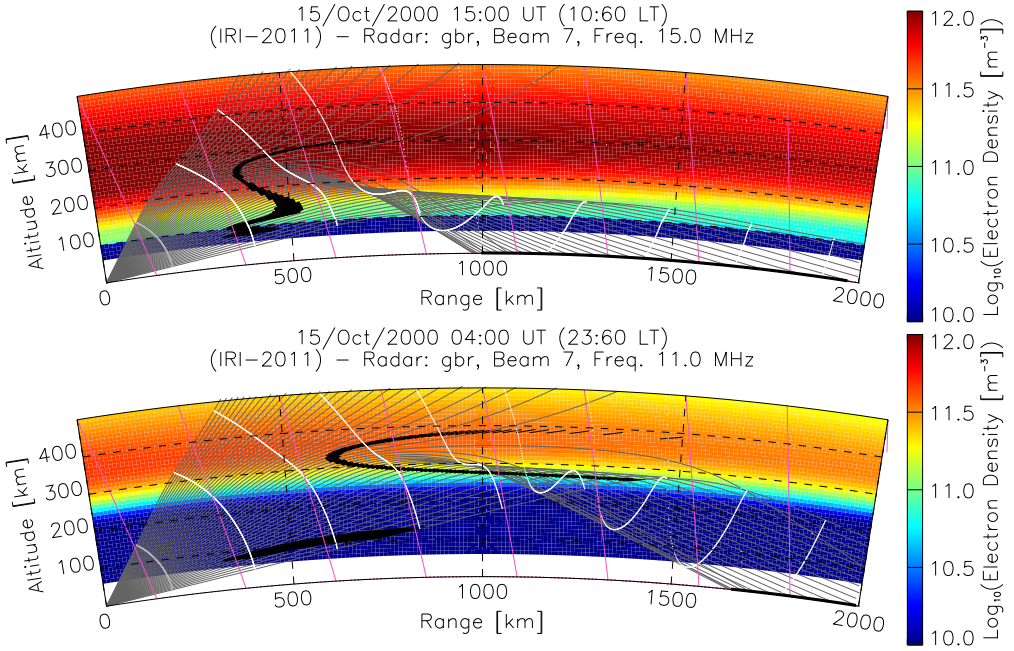

Figure 1.3: Propagation of HF radio waves during daytime (top) and nighttime (bottom) conditions using the 2011 International Reference Ionosphere (IRI-2011) model. Gray lines represent transmitted ray paths, pink lines are geomagnetic field lines, white lines are regularly spaced slant range intervals, and black markers are regions of backscatter from either field-aligned plasma irregularities or the Earth's surface.

above E region altitudes. High Frequency (HF) systems are capable of using ionospheric refraction to observe Bragg scattering from decameter-scale plasma irregularities in both the E and F region high-latitude ionosphere [*Greenwald et al.*, 1995; *Ballatore et al.*, 2001].

Two cases for HF propagation of radio waves in the high-latitude ionosphere are considered in Figure 1.3. The 2011 International Reference Ionosphere (IRI-2011) model is used to generate two-dimensional ionospheric profiles for daytime (top) and nighttime (bottom) scenarios on October 15, 2000. Gray lines represent individual ray paths transmitted from a point on the ground over an elevation range from 5° to 55°, while white lines mark regularly spaced range intervals. Regions where rays either achieve orthogonality to geomagnetic field lines (pink lines) or scatter from the Earth's surface are shaded black. For the daytime case in the top panel of Figure 1.3, the majority of rays are refracted to the Earth's surface and

are unable to penetrate the ionosphere to achieve orthogonality to field lines within the F region peak near 350 km altitude. In the bottom panel, transmitted rays are able to achieve orthogonal scattering conditions within two regions of the nighttime ionosphere. The first is from the E region below 150 km altitude and between about 400–800 km in range from the HF source. The second is in the F region at altitudes from 250–400 km and between about 600–1400 km in range from the source. At further ranges ($>$ 1600 km) rays are shown scattering from only the Earth's surface. If the ray-tracing environment is extended to further ranges, some of these rays will eventually achieve orthogonality to field lines after forward scattering from the ground. These two examples demonstrate how HF radio waves can backscatter from both field-aligned plasma density irregularities and the Earth's surface under daytime and nighttime ionospheric conditions.

1.2 SuperDARN

The modern inspiration for the Super Dual Auroral Radar Network (SuperDARN) can be traced back to an experiment performed in April 1973 using a pair of Very High Frequency (VHF) coherent radars with fixed, overlapping beams near Anchorage, Alaska [*Ecklund et al.*, 1975]. These radars measured the line-of-sight (LOS) Doppler velocities associated with field-aligned irregularities at E region altitudes. Simultaneous observations from common scattering volumes showed that the LOS Doppler shift varied as a function of azimuth while the spectral width components remained constant. Following this experiment's success, in January 1979 a new pair of bistatic VHF radars was operated in Scandinavia as part of the Scandinavian Twin Auroral Radar Experiment (STARE). The two radars used phased-array receive antennas to electronically steer through 8 overlapping beams with a common-volume area of about 400×400 km to resolve two-dimensional velocities of field-aligned plasma irregularities [*Greenwald et al.*, 1978]. A temporary radar was then constructed near Fairbanks,

Alaska in February 1982 to test the effectiveness of high-frequency (HF) signals for the study of F region small-scale irregularities at high-latitudes. This experiment showed that observed field-aligned irregularity drifts followed the expected motion of the high-latitude convection pattern and were not impacted by characteristic frequencies such as the ion cyclotron lines [*Greenwald et al.*, 1983]. Aspects from each of these radar experiments, including common volume measurements and operation at HF frequencies, would be retained for future radar designs.

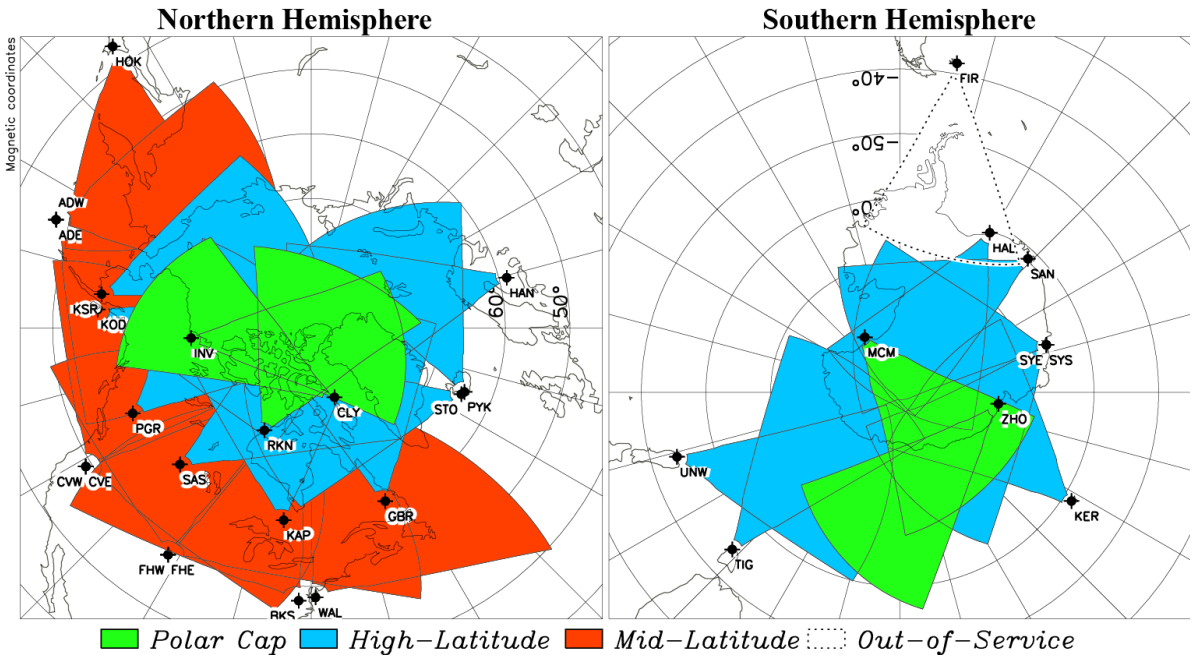

Figure 1.4: Fields of view of currently operational SuperDARN radars in northern (left) and southern (right) hemispheres. Mid-latitude, high-latitude, and polar radar FOVs are shaded red, blue, and green respectively.

The first SuperDARN radar was constructed in Goose Bay, Labrador and saw first light in October 1983 [*Greenwald et al.*, 1985]. The Goose Bay radar is still in operation and continuously measures LOS velocities, spectral width, and backscattered power from decameter-scale field-aligned plasma irregularities in the F region ionosphere. The main antenna array consists of 16 horizontal log-periodic antennas which transmit and receive

signals over a frequency range from 8-20 MHz. A similarly-designed HF radar was constructed in January 1988 at Halley Station in Antarctica to study the interhemispheric conjugacy of ionospheric phenomena. Attempting to replicate the common volume measurements from the earlier STARE experiment, an HF radar was installed at Schefferville, Quebec 500 km away from the Goose Bay site. This experiment demonstrated the ability to resolve two-dimensional convection velocities from common-volume observations at HF frequencies, although it was found that the spacing between radars was insufficient for precise vector determination at higher latitudes. The Schefferville radar was eventually dismantled and used to supplement the construction of a new SuperDARN radar in Stokkseyri, Iceland for better common-volume measurements with the Goose Bay radar [*Greenwald et al.*, 1995].

In its present state, the SuperDARN network consists of a total of 30 radars operated by over a dozen institutions around the world (Figure 1.4). The names and geographic locations of all of the radars in the Northern and Southern Hemispheres are listed in Table 1.1 and Table 1.2. All radars generate common data products so that LOS velocity measurements can be combined into global maps of ionospheric plasma convection [*Ruohoniemi and Baker*, 1998]. Under the current SuperDARN Principal Investigator (PI)'s Agreement, data from each individual radar site is first sent to The Johns Hopkins Applied Physics Laboratory for ingestion and fusion before being sent to the University of Saskatchewan for final copying and distribution to each of the PI institutions. Further discussion of SuperDARN operating characteristics and the generation of these convection patterns can be found in Section 3.2.1 [*Chisham et al.*, 2007].

Table 1.1: List of current SuperDARN radars in the Northern Hemisphere.

Radar Name	**Geog. Lat.** [°]	**Geog. Lon.** [°]	**Start Year**
Adak Island East	51.88	-176.62	2012
Adak Island West	51.88	-176.62	2012
Blackstone	37.10	-77.95	2008
Christmas Valley East	43.27	-120.36	2011
Christmas Valley West	43.27	-120.36	2011
Clyde River	70.49	-68.50	2012
Fort Hays East	38.86	-99.39	2009
Fort Hays West	38.86	-99.39	2009
Goose Bay	53.32	-60.46	1983
Hankasalmi	62.32	-26.61	1995
Hokkaido	43.33	143.61	2006
Inuvik	68.42	-133.5	2008
Kapuskasing	49.39	-82.32	1993
King Salmon	58.68	-156.65	2001
Kodiak	57.62	-152.19	2000
Pykkvibaer	63.77	-20.54	1995
Prince George	53.98	-122.59	2000
Rankin Inlet	62.82	-93.11	2006
Saskatoon	52.16	-106.53	1993
Stokkseyri	63.86	-22.02	1994
Wallops Island	37.93	-75.47	2005

Table 1.2: List of current SuperDARN radars in the Southern Hemisphere.

Radar Name	**Geog. Lat.** [°]	**Geog. Lon.** [°]	**Start Year**
Halley	-75.52	-26.63	1988
Kerguelen	-49.22	70.14	2000
McMurdo	-77.88	166.73	2010
SANAE	-71.68	-2.85	1997
Syowa East	-69.00	39.58	1997
Syowa South	-69.00	39.58	1997
Tiger	-43.40	147.20	1999
Unwin	-46.51	168.38	2004
Zhongshan	-69.38	76.38	2010

1.3 Global Positioning System

The concept of a satellite navigation system was first proposed after the launch of Sputnik 1 on October 4, 1957. Scientists at The Johns Hopkins Applied Physics Laboratory were able to trace the orbit of the spacecraft by measuring the Doppler shift in the frequency of its continuously transmitted signal [*Guier and Weiffenbach*, 1960]. Soon afterward in 1959, the U.S. Navy launched the first satellite for a two-dimensional navigation system known as the Navy Navigation Satellite System (NAVSAT) or TRANSIT. These spacecraft were located at an altitude of about 1,000 km with an orbital period of roughly 100 minutes and transmitted navigation messages at 150 and 400 MHz. Users on the Earth's surface were able to calculate their location to an accuracy of only about 50-200 km and each satellite remained in view for no more than 20 minutes at a time. Because navigation signals were transmitted on two different frequencies, users were able to estimate delays introduced by electron densities in the ionosphere by measuring the difference in the arrival time of the two received signals. This novel concept would be re-used for later satellite navigation systems. The TRANSIT system was fully operational with a total of 7 satellites and 6 spares in orbit from 1968 until its retirement in 1996 [*Yionoulis*, 1998].

To overcome the shortcomings of TRANSIT, a new satellite navigation system was developed by Aerospace Corp. and the Department of Defense (DoD) Joint Program Office (JPO) called the Global Positioning System (GPS). GPS differed from TRANSIT in two key aspects: each spacecraft carried four atomic clocks for highly accurate time synchronization, and users were able to calculate a fully three-dimensional navigation solution by solving a series of four independent equations for the receiver clock bias and their three position coordinates. Each satellite transmitted its ephemeris and timing information on the same two frequencies: L1 (1575.42 MHz) and L2 (1227.6 MHz). Pseudorandom noise codes (PRNs)

called the precision (P) code and coarse acquisition (C/A) code are modulated onto these two signals. The L1 and L2 signals are modulated by the P-code while only the L1 signal is modulated by the C/A code (Figure 1.5). The DoD encrypted the P code to ensure the most accurate navigation solutions would be reserved for military personnel. An intentional degradation called selective availability was also imposed on the C/A code available to civilian users which created navigation errors on the order of hundreds of meters. The first Block-I GPS satellite was launched in 1978, with additional spacecraft regularly launched until a fully operational constellation of 24 satellites was achieved in 1993 [*Getting*, 1993].

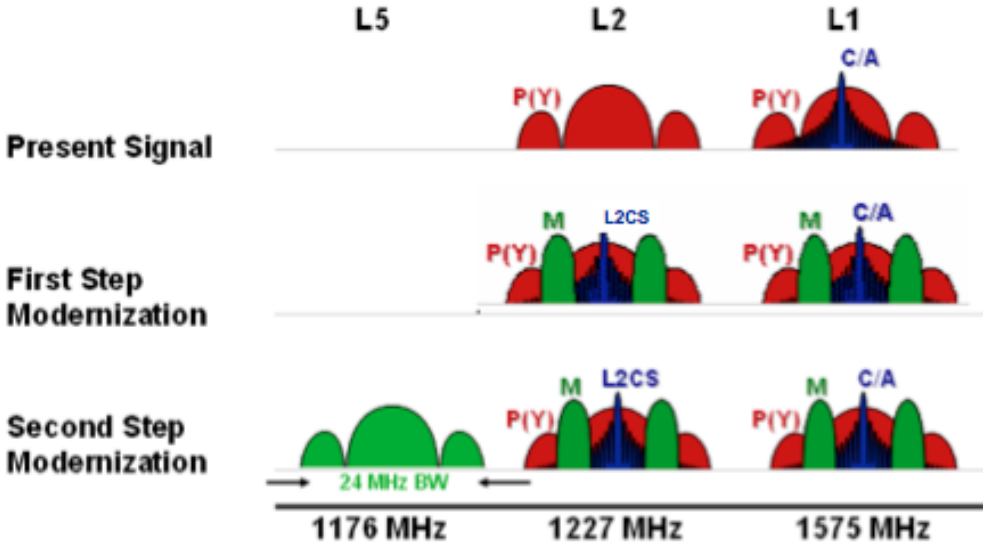

Figure 1.5: Modernization of GPS signals. "Present Signal" refers to the signal structure at the time of the constellation's completion in 1995 [*Coster*, 2011].

In its present state, the GPS constellation consists of between 24 and 32 satellites in six orbital planes with an inclination of 55°. The spacecraft orbits are nearly circular and are located 26,600 km from the center of the Earth. The control segment for GPS consists of a master control station (MCS) at Schriever Air Force Base, an alternate MCS, and six monitor stations at accurately-located geographic positions. Selective availability was permanently turned off on May 4, 2000 by Executive Order from President Clinton [*Kintner*, 1999].

A modernization process is underway to improve the quality of signals available to both military and civilian users with several new PRN codes modulated on the L1 and L2 signals (Figure 1.5). In addition, a new L5 signal at 1776.45 MHz will be available to civilian users for support of safety-of-life applications. A modified Block IIRM spacecraft launched on March 24, 2009 is the first GPS satellite to transmit the new L5 signal [*Shaw et al.*, 2000; *Coster*, 2011].

1.4 Thesis Organization

The purpose of this thesis is to present the ongoing research work combining ionospheric measurements from ground-based GPS receivers and SuperDARN HF radars (Chapter 2 & Chapter 3), with one chapter devoted to the capability of SuperDARN radars to study the Earth's surface (Chapter 4). In Chapter 2, the theory and application of GPS total electron content are discussed, as well as an anomalous feature discovered at mid-latitudes over North America. The interactive online plotting tools available at the Virginia Tech SuperDARN website are also introduced. In Chapter 3, the role of convection electric field in the formation of a polar tongue of ionization from mid-latitude storm enhanced density is presented using measurements from both SuperDARN HF radars and ground-based GPS receivers in manuscript format. In Chapter 4, the influence of ground surface effects on SuperDARN observations due to sea ice cover for selected Northern Hemisphere radars are presented. Finally, in Chapter 5 conclusions and ideas for future work are discussed.

Chapter 2

GPS Total Electron Content

2.1 Introduction

Total electron content (TEC) is a commonly-used parameter for characterizing the Earth's ionosphere. It is defined as the total number of electrons within a cross-sectional volume along a path between two points and given in units of 1×10^{16} electrons/m^2, or 1 TECU. To calculate TEC from a ground-based GPS receiver one must first understand the propagation of an electromagnetic (EM) wave in a weakly ionized plasma such as the Earth's ionosphere. Figure 2.1 shows a diagram demonstrating the effect of the ionosphere on a GPS signal. The speed of an EM wave is described by both its phase velocity and group velocity. Phase velocity is the speed of a point of constant phase on the wave; for an EM wave travelling through the ionosphere the phase velocity is given as

$$v_\phi = \frac{\omega}{k} = \frac{c}{n} = \frac{c}{\sqrt{1-\omega_{pe}^2/\omega^2}}$$

where c is the speed of light, ω is the wave frequency, k is the wave number, and the plasma frequency $\omega_{pe} = n_e q^2/\varepsilon m_e$. The electron density n_e is the only environmental parameter contributing to plasma frequency; the other variables are all constants. Because the index of refraction in the ionosphere is always less than 1, the phase velocity is always equal to or

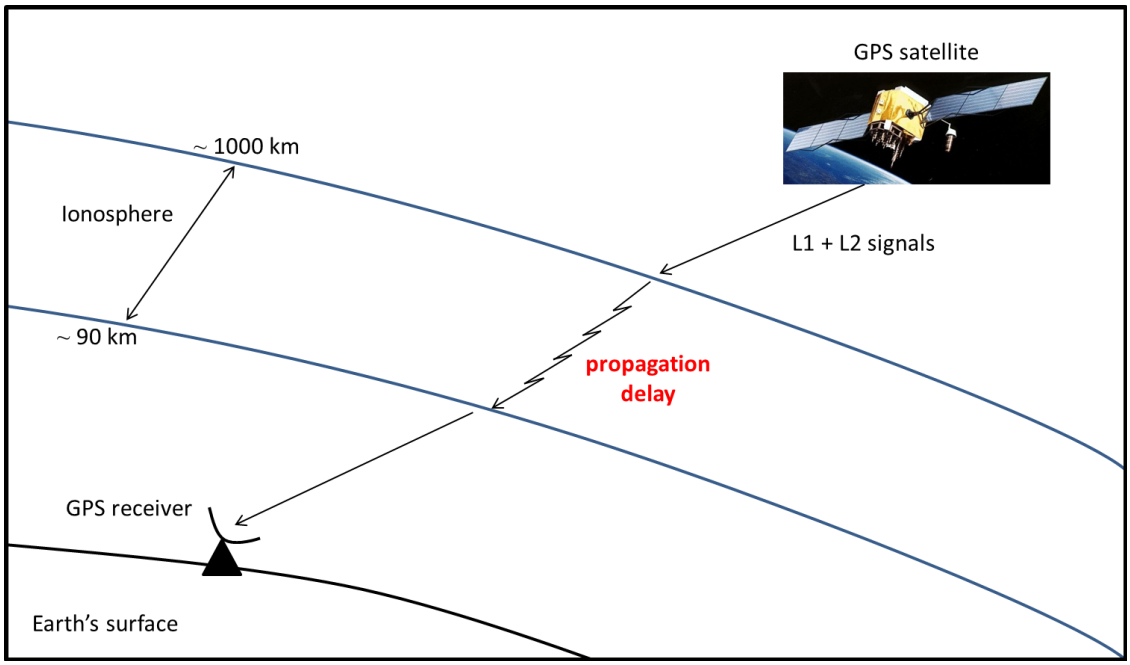

Figure 2.1: Diagram showing propagation delays introduced on GPS signals by the Earth's ionosphere.

greater than the speed of light. The group velocity of the EM wave is given as

$$v_g = \frac{d\omega}{dk} = c\sqrt{1 - \frac{\omega_{pe}^2}{\omega^2}}$$

and is always less than or equal to the speed of light. For the case of an L1 GPS signal (1575.42 MHz) the wave frequency ω is much greater than the typical daytime ionospheric plasma frequency of 10 MHz, such that the group velocity can be approximated as

$$v_g = c\left(1 + \frac{\omega_{pe}^2}{2\omega^2}\right)$$

The speed of the C/A code modulated on the L1 carrier will always be less than the speed of light as it passes through the Earth's ionosphere. The time delay δt can be calculated

from the group velocity as

$$\delta t = \frac{1}{c} \int\limits_{path} \frac{\omega_{pe}^2}{2\omega^2} dr$$

Removing all of the constants from inside the integral, only the electron density n_e is left to be integrated along the propagation path:

$$\delta t = \frac{q^2}{2c\varepsilon m_e f^2 (2\pi)^2} \int\limits_{path} n_e(r) dr = \frac{40.3}{cf^2} TEC$$

where f is the wave frequency in Hz and TEC is the total electron content along the path. Although δt cannot be measured at one frequency with a standard receiver clock, it is possible to measure the difference in arrival times of the L1 and L2 signals. Solving for TEC,

$$TEC = \frac{c}{40.3} \frac{f_{L1}^2 f_{L2}^2}{f_{L1}^2 - f_{L2}^2} (\delta t_{L2} - \delta t_{L1})$$

Researchers at MIT Haystack Observatory maintain one of several databases of global TEC (NASA Jet Propulsion Laboratory in California and the National Institute of Communications Technology in Japan are two others). The group at MIT Haystack was the first to incorporate GPS receivers from outside the International GNSS Service (IGS) and Continuously Operating Reference System (CORS) networks of strictly-managed receivers to identify plumes of storm enhanced density (SED) that form over the United States during geomagnetic storms [*Coster et al.*, 2001]. Data files in RINEX and other formats are downloaded from thousands of GPS receiver sites around the world for automated processing with the MIT Automated Processing of GPS (MAPGPS) software package. First, a multiplicative factor called a mapping function is used to convert each individual line-of-sight TEC measurement into a zenith TEC estimate. An ionospheric pierce point at 350 km altitude is assumed and an elevation angle cutoff of 7° is imposed. The mapping function used in the

automated processing is:

$$z = \frac{1}{\sqrt{(1.0 - (F\cos(el))^2)}}$$

where the adjustment parameter, F, is set to 0.95 for minimization of the average difference in estimated zenith TEC values for coincident measurements. After the conversion to zenith TEC values, a combination of three different techniques is used for the estimation and removal of receiver biases: minimum scalloping, least squares, and the zero TEC method. A detailed explanation of these three methods can be found in *Rideout and Coster* [2006]. Finally, after receiver biases have been accounted for the original data stream is decimated to a lower rate for faster processing time. Since June 2005, maps of global GPS TEC have been available from the Madrigal website at MIT Haystack (http://madrigal.haystack.mit.edu/madrigal). Data is provided at 5-minute intervals in 1° by 1° cells in geographic coordinates [*Rideout and Coster*, 2006; *Coster*, 2011]. Sample maps of TEC data averaged over 20-minute intervals into 3° by 3° bins are posted on that day's experiment page.

A collection of application programming interfaces (APIs) have been developed for remotely accessing data stored on Madrigal. These APIs are available for use with Python, Matlab, IDL, and Mathematica and are freely available online from the Madrigal website (http://madrigal.haystack.edu/madrigal/madDownload.html). Because an ASCII file from Madrigal containing TEC data for a single day generally exceeds 100 MB, an effort was made to reduce these file sizes. A script using the IDL APIs and the "writeu" command is responsible for downloading, converting, and storing GPS TEC data in a compressed, unsigned binary format to a local computer. This results in a reduction in file size by about 95%. Once the quality of this file has been verified, it is transferred to the main VT SuperDARN data server for general access. Figure 2.2 compares the data downloaded directly from Madrigal to a sample image hosted on the experiment page for August 4, 2010.

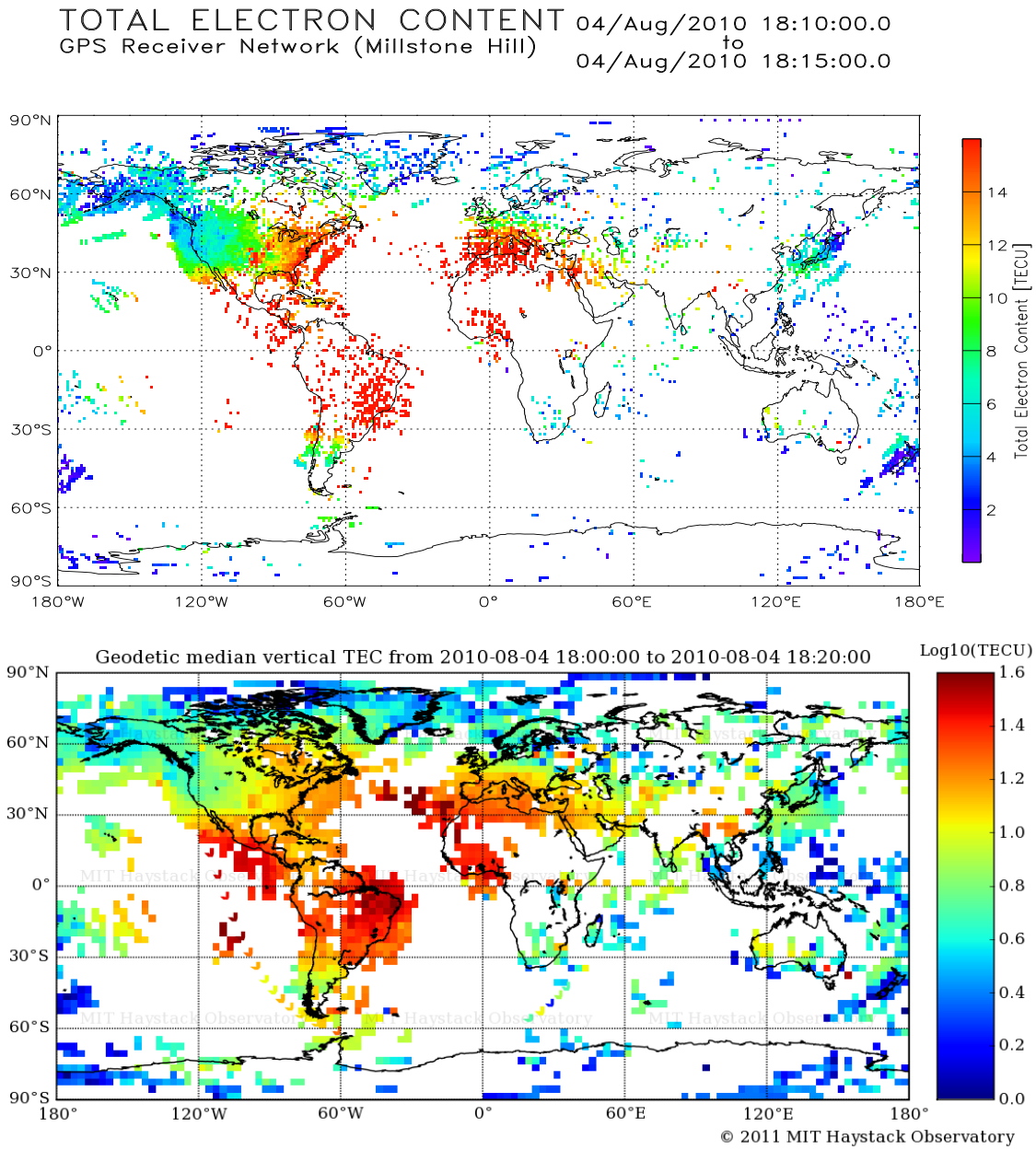

Figure 2.2: Comparison of GPS TEC plots on VT SuperDARN (top) and Madrigal (bottom) websites for the period around 18:10 UT on August 4th 2010. Significant differences are the longer time integration, larger spatial averaging, and logarithmic color scale used in the Madrigal plot.

2.2 Online Plotting Tools

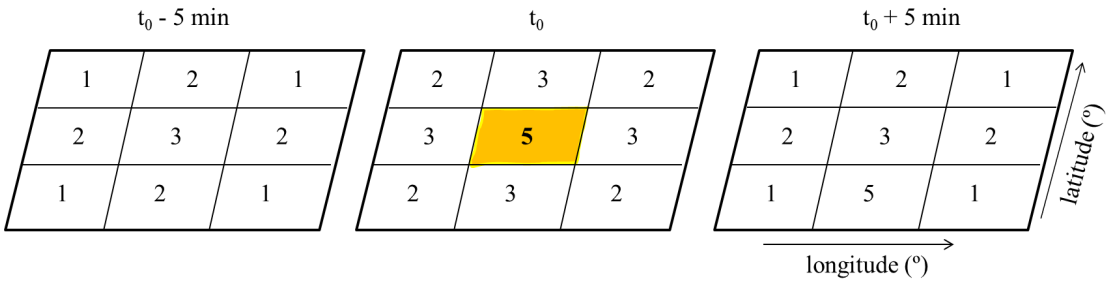

Figure 2.3: Diagram of the median filtering grid with cell weights identified. Highlighted cell is the latitude/longitude bin currently being checked against the user-defined threshold value.

Due to the sparse GPS receiver coverage in some areas, a spatiotemporal median filtering technique is sometimes applied to the TEC data after it has been downloaded from Madrigal. This process examines both spatially and temporally adjacent bins to determine whether enough real data values are present for a certain bin to be turned on (Figure 2.3). TEC data is first re-binned into a user-defined latitude/longitude grid in geomagnetic coordinates (typically 1° latitude by 2° longitude). For each new latitude/longitude bin, the routine checks for the presence of real TEC values within a 3° × 3° grid. Adjacent cells in the current 5-minute TEC map are given the greatest weight; adjacent cells in the previous and following 5-minute maps are given smaller weights. If the sum of the weights of all cells with TEC data divided by the sum of the weights of all the cells in the grid (55) exceeds a certain threshold, then the median value from the adjacent cells is used; otherwise, that cell's value is set to zero. This process is repeated for all latitude/longitude bins within the hemisphere of interest. A cutoff at 85° geomagnetic latitude is imposed to avoid issues with increasingly smaller spatial bins near the poles. The influence of varying threshold values can be seen in Figure 2.4; threshold values between 0.10 and 0.30 are typically used.

A package of online plotting tools has been developed for easy generation of combined

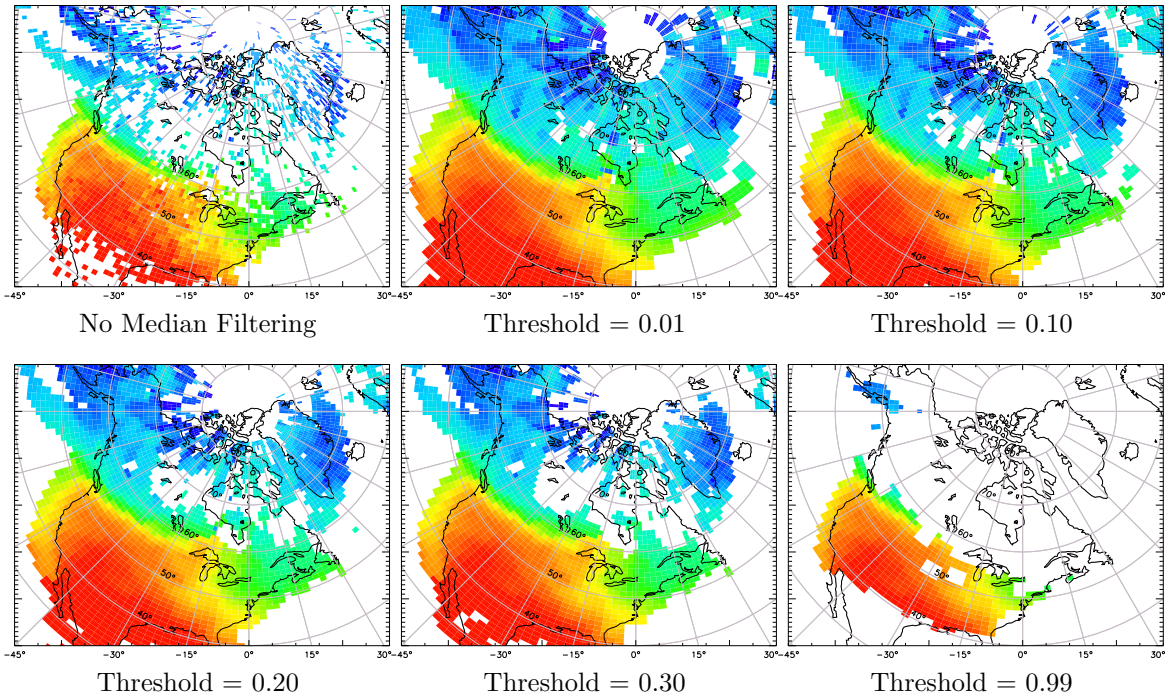

Figure 2.4: Examples of different median filtering threshold values and their comparison to the original GPS TEC data as downloaded from Madrigal. Figures are plotted in geomagnetic coordinates.

GPS TEC/SuperDARN figures. The first and most widely used of these tools is called the TEC Four Plot (Figure 2.5). The upper left panel shows "unfiltered" GPS TEC data as it is downloaded from Madrigal and plotted using a linear color scale. The lower left panel shows "median filtered" GPS TEC data plotted using a linear color scale. Users are able to define the size of the re-gridded latitude/longitude bins as well as the median filtering threshold value. When selected, SuperDARN convection patterns are overlaid only in this frame. The upper right panel shows either single or five-minute scans of SuperDARN backscatter velocity measurements. For single scans, the actual scan time is given along the upper left side of the panel. Finally, the lower right panel shows SuperDARN backscatter power measurements overlaid on a grayscale map of GPS TEC data. The size of the backscatter symbols are scaled according to power. Checkboxes allow users to turn on and off line-of-sight measurements

from as many radars in the particular hemisphere as they wish. By default the perspective is fixed over North America for optimal viewing of the new mid-latitude chain of SuperDARN radars, although users are given the option to change the area to be plotted, switch coordinate frames, and select between different hemispheres. After generating one of these four plots a link to that day's GPS TEC data file on Madrigal can be found below the figure. If no data for the selected date are available, the user receives an error message and a link to a summary plot of the available TEC data on Virginia Techs servers is provided.

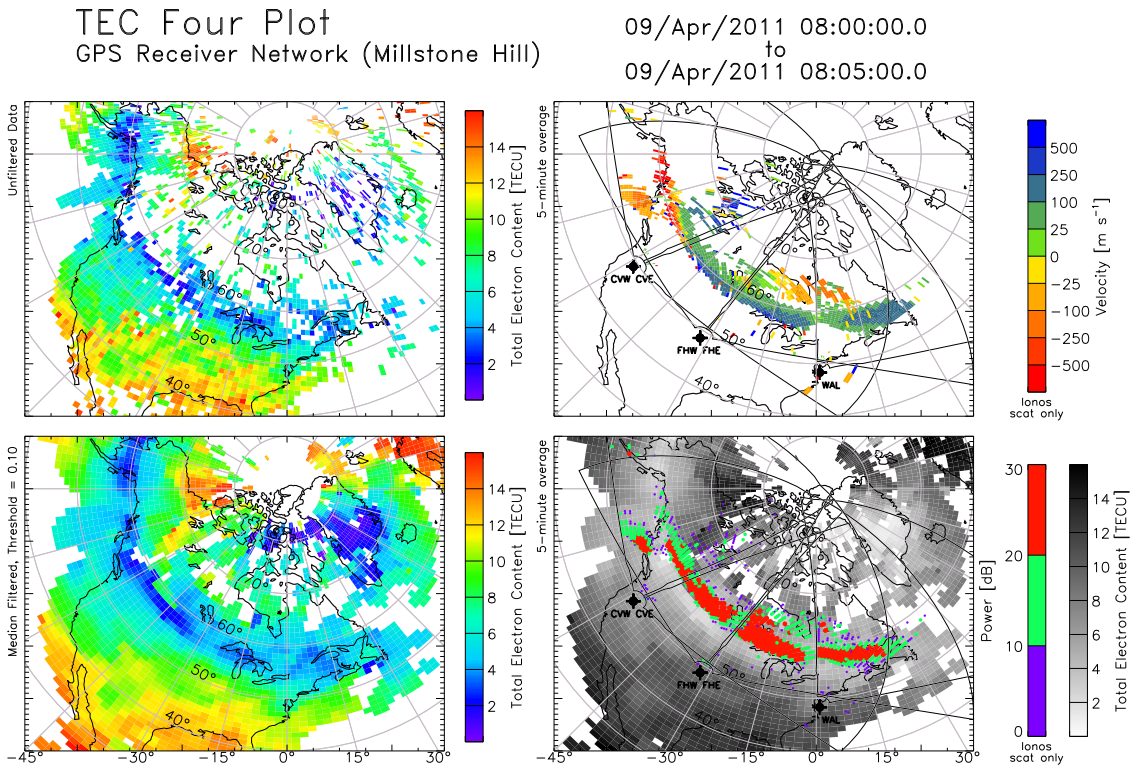

Figure 2.5: Output from the GPS/TEC Plotting - Four Plot page on the VT SuperDARN website for a SAPS event on April 9, 2011.

2.3 Seasonal Variations and a North American Anomaly

The primary motivation for developing these new plotting tools is to examine geomagnetically disturbed conditions in the ionosphere. However, before considering stormtime features we must first gain an understanding of "normal" TEC values during geomagnetically quiet periods. For this analysis, the planetary Kp index is used to differentiate between quiet and disturbed conditions. The Kp index represents the mean value of the disturbance levels in the two horizontal magnetic field components within a 3-hour interval measured at 13 subauroral ground stations. The criteria Kp < 2.0 is used for selecting geomagnetically quiet periods. Monthly TEC averages over North America are calculated for each hour using only the days when Kp < 2.0 during the interval of interest. Figure 2.6 shows monthly averages for Kansas local noon (19:00 UT) and midnight (07:00 UT) during March, June, September, and December in 2008. The number of days in the month being included in the average is shown in the upper left of each panel. As expected, TEC values over North America are lower at midnight than on the dayside at noon. The average noon values for March 2008 are signifcantly higher than the other seasons, which could be explained by the fewer number of days being included in the averaging process.

An anomalous GPS TEC feature was observed while trying to characterize average TEC values over North America during quiet geomagnetic conditions (March/midnight and September/noon panels in Figure 2.6). This anomaly appears over the central United States as an enhancement of about 3-5 TECU above the background densities. Discussions with the principal investigator of the GPS TEC dataset at MIT Haystack confirm that this feature is in fact a geophysical phenomenon and not an artifact of bad data from receiver sites. One proposed mechanism for this anomaly is the zonal wind–magnetic declination effect which causes large longitudinal variations in electron density over the continental United

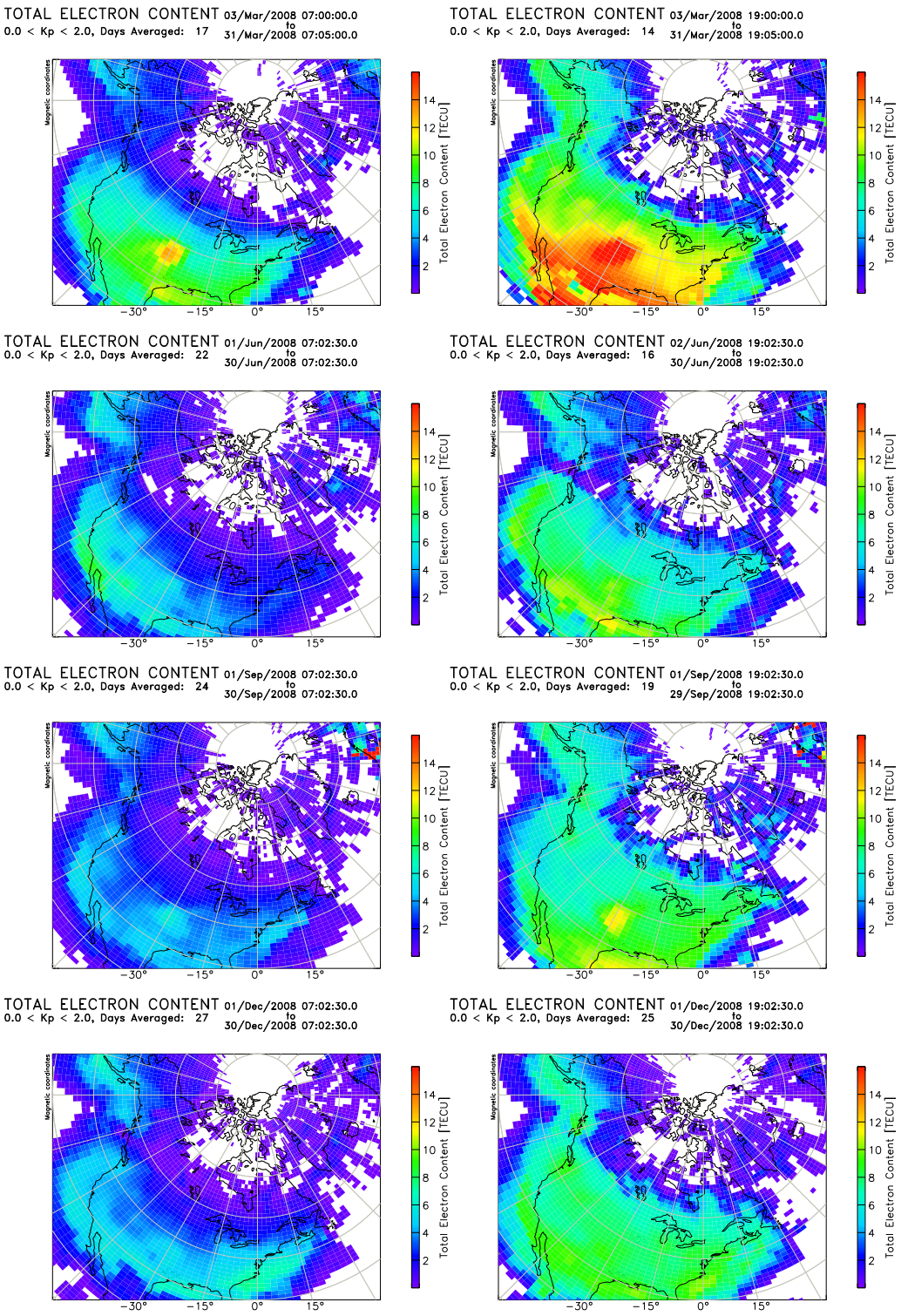

Figure 2.6: Seasonal variations in average GPS TEC over North America during geomagnetically quiet conditions (Kp < 2.0) for March, June, September, and December 2008. Columns correspond to Kansas local midnight (07:00 UT, left) and noon (19:00 UT, right).

States [*Zhang et al.*, 2012]. Figure 2.7 demonstrates how an eastward zonal wind will push ions upward along magnetic field lines over the eastern United States and into regions where recombination rates are lower. The opposite is true over the western United States where ions are pushed downward along field lines to lower altitudes where recombination rates are higher, thus leading to lower electron densities and a decrease in TEC. It could be possible that some orientation of zonal winds produce a localized uplift to altitudes with lower recombination rates, allowing for the anomaly feature to persist for an extended period of time.

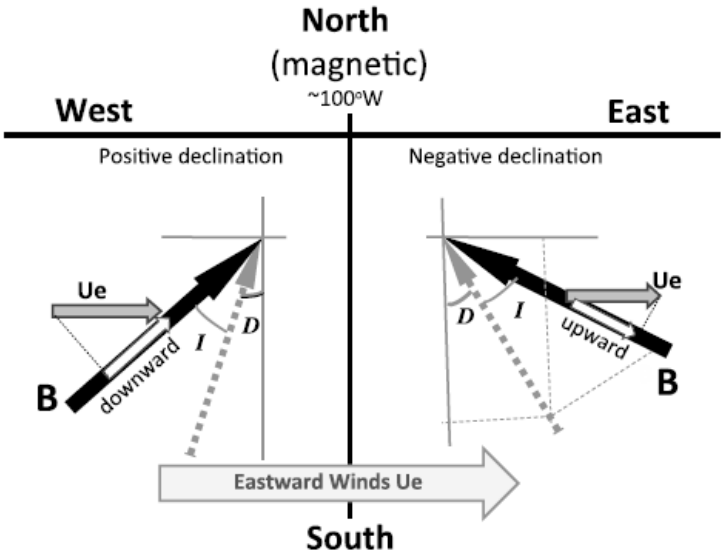

Figure 2.7: Diagram of geomagnetic declination and the effect of an eastward zonal wind on longitudinal variations in electron density. Magnetic field lines are into the sheet plane with dip angles I, and the sheet plane is the horizontal plan stretching into east and west, and north and south. Center vertical line represents the longitudes with zero magnetic declination. Magnetic field lines have declination D, which is positive (eastward) on the west side of the zero declination, and is negative (westward) on the east side [*Zhang et al.*, 2012].

An automated search algorithm has been developed in an attempt to track the occurrence of this phenomenon. First, the algorithm finds the median TEC value within a bounded region for a 5-minute interval. This region ($20° \leq$ lat. $\leq 50°$ and $-120° \leq$ lon. $\leq -80°$, Figure 2.8) was selected based on visual inspection of the typical anomaly location. Next, the average percentage difference between all cells within this region and the median value

of the entire region is calculated. Once this process has been repeated for each 5-minute TEC map for a day, the median of all the average percentage differences is assigned to that day. This method is intended to indicate dates when there is a discrete region of enhanced TEC within the bounded area.

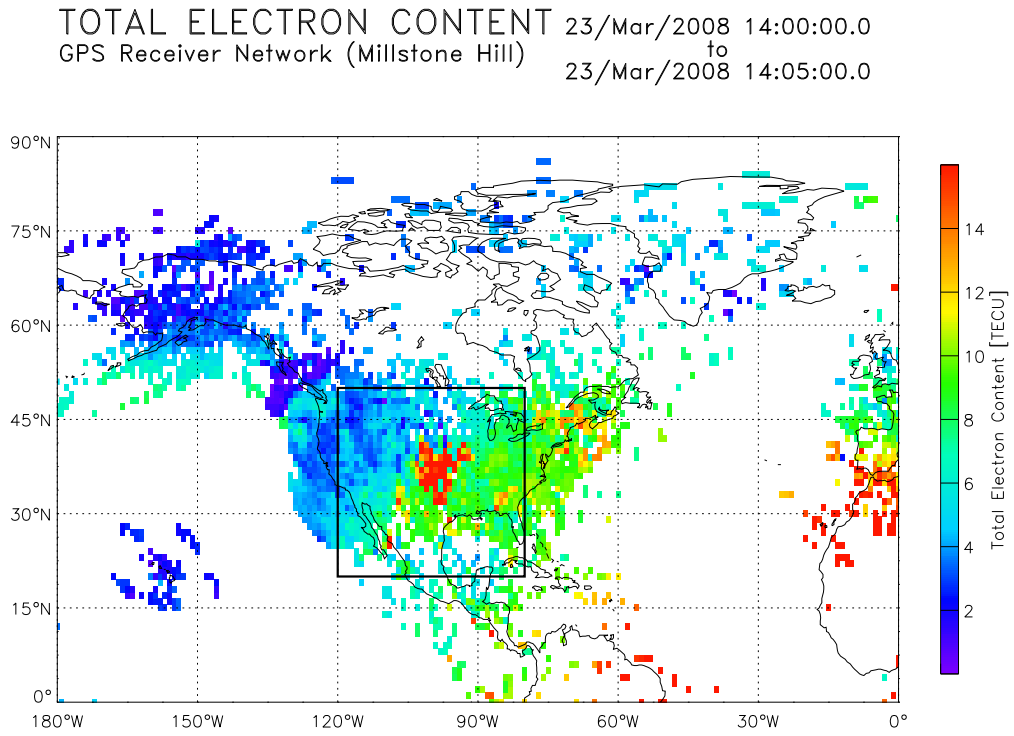

Figure 2.8: GPS TEC anomaly observed over North America at mid-latitudes on March 23rd, 2008 at 14:00 UT. The boxed region shows the latitudinal and longitudinal extent considered by the automated anomaly search function.

The results from this search algorithm can be seen in Figure 2.9 and Figure 2.10 for the years 2008 and 2009 respectively. Percent differences of at least +6% tend to agree very well with anomaly occurrence as determined by visual inspection of plots. One of the main conclusions is that fewer occurrences of the anomaly are observed in 2009 than 2008. Further analysis indicates that the anomaly has been seen less often in each successive year since 2008, suggesting an inverse relationship with approaching solar maximum. The anomaly also appears much less frequently in winter months. This search algorithm will need to

be applied to more years of data to prove or disprove any solar cycle dependence. It will also be necessary to determine whether there are any local time effects on the algorithm's effectiveness (i.e. whether the enhancement is less noticeable during daytime due to increased background densities).

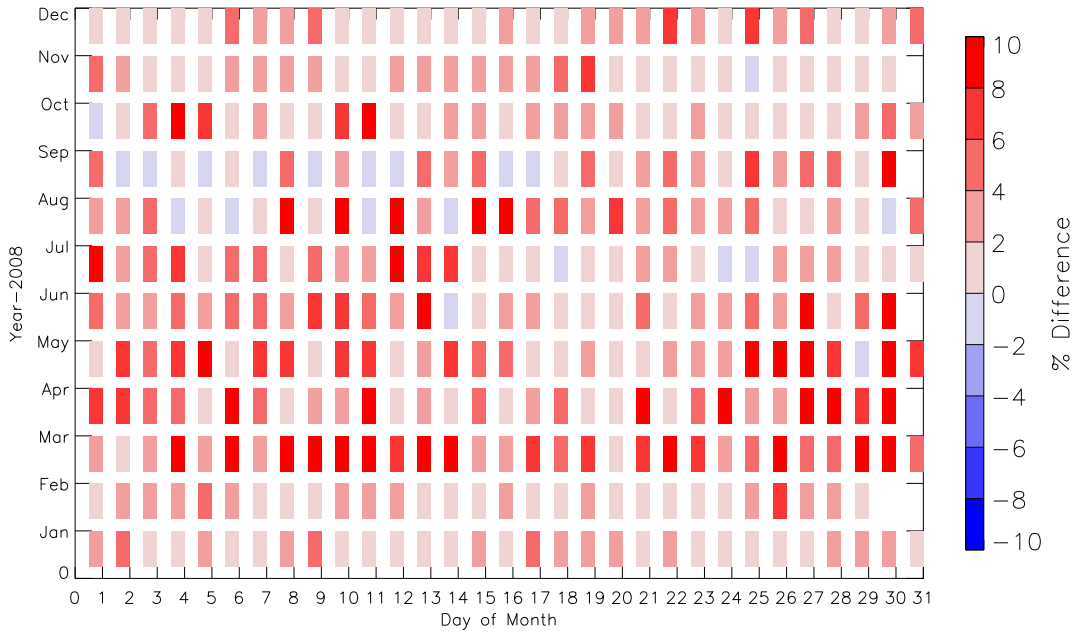

Figure 2.9: Results from automated search routine for North American anomaly for all days of year 2008. Median percent differences above +6% correspond to anomaly occurrence within the bounded search region.

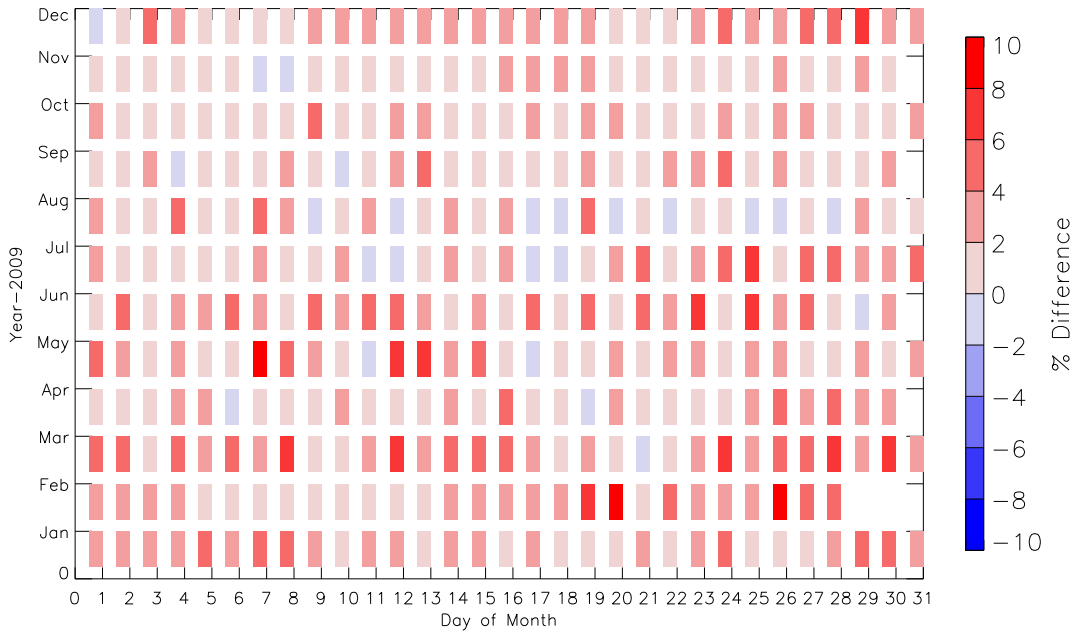

Figure 2.10: Results from automated search routine for North American anomaly for all days of year 2009. Median percent differences above +6% correspond to anomaly occurrence within the bounded search region.

2.4 Summary

We have presented ionospheric total electron content (TEC) data and described how to calculate it from the group delays of the L1 and L2 GPS signals as they pass through the ionosphere from a satellite to a receiver on the ground. Researchers at MIT Haystack Observatory process line-of-sight TEC measurements from thousands of ground-based GPS receivers around the world to create globally gridded maps of zenith TEC values assuming ionospheric pierce points at 350 km altitude. This data is downloaded from the Madrigal database and stored on the VT SuperDARN servers in a compressed, unsigned binary format. A variety of online plotting tools have been developed for direct comparison of SuperDARN and GPS TEC data , including the TEC Four Plot (http://vt.superdarn.org/tiki-index.php?page=DaViT+TEC+Four+Plot). Using these tools, we have attempted to characterize typical TEC values during geomagnetically quiet conditions for better understanding of stormtime effects. Maps of average monthly TEC have been calculated and lead to the identification of a recurrent localized enhancement of TEC over the central United States. The interaction between zonal winds and the reversal in magnetic declination over North America has been suggested as a possible source mechanism. An automated search algorithm has been implemented in an attempt to characterize the anomaly's frequency of occurrence for the years 2008 and 2009. The anomaly tends to appear less frequently since 2008 with approaching solar sunspot maximum and is most commonly observed in spring and summer months. Further analysis of solar cycle and local time dependence and their relationship to zonal winds will be performed to determine the driving mechanisms behind this TEC anomaly.

Chapter 3

Direct observations of the role of convection electric field in the formation of a polar tongue of ionization from storm enhanced density

E. G. Thomas[1], J. B. H. Baker[1], J. M. Ruohoniemi[1], L. B. N. Clausen[1,2], A. J. Coster[3], J. C. Foster[3], P. J. Erickson[3], JGR, under revision, November 2012.

Abstract

We examine the relationship of convection electric fields to the formation of a polar cap tongue of ionization (TOI) from mid-latitude plumes of storm enhanced density (SED). Observations from the geomagnetic storm on 26-27 September 2011 are presented for two distinct SED events. During an hour-long period of geomagnetic activity driven by a coronal mass ejection, a channel of high density F region plasma was transported from the dayside subauroral ionosphere and into the polar cap by enhanced convection electric fields extending to middle latitudes. This TOI feature was associated with enhanced HF backscatter, indicating that it was the seat of active formation of small-scale irregularities. After the solar wind IMF conditions quieted and the dayside convection electric fields retreated to higher latitudes, an SED plume was observed extending to, but not entering, the dayside cusp region. This prominent feature in the distribution of total electron content (TEC) persisted for several hours and elongated in magnetic local time with the rotation of the Earth. No ionospheric scatter from SuperDARN radars was observed within this SED region. The source mechanism (enhanced electric fields) previously drawing the plasma from mid-latitudes and into the polar cap as a TOI was no longer active, resulting in a fossil feature. We thus demonstrate the controlling role exercised by the convection electric field in generating a TOI from mid-latitude SED.

3.1 Introduction

The plasma of Earth's ionosphere at high latitudes is subject to redistribution by strong electric fields of magnetospheric origin. At F region altitudes centered on 200-400 km both ions and electrons drift with a nearly horizontal velocity given by $\mathbf{v} = \mathbf{E}\times\mathbf{B}/\mathrm{B}^2$, where $\mathbf{E}$ is the ionospheric electric field and $\mathbf{B}$ is the geomagnetic field. The large-scale motion of the plasma most often conforms to a two-cell pattern, with antisunward flow from the dayside across the polar cap to the nightside and return flow at auroral latitudes in the dawn and dusk sectors [*Heppner and Maynard*, 1987; *Ruohoniemi and Greenwald*, 1996].

A tongue of ionization (TOI) is a channel of high-density F region plasma transported from the dayside mid-latitude ionosphere through the cusp and into the polar cap by enhanced convection electric fields [*Sato*, 1959; *Sato and Rourke*, 1964; *Knudsen*, 1974]. Storm enhanced density (SED) is a plume of ionization in the dusk sector that is carried sunward and poleward by the low-latitude edge of the subauroral polarization stream (SAPS) [*Foster et al.*, 2004; *Foster and Burke*, 2002; *Foster and Vo*, 2002] during major disturbances. Both features are characterized by enhanced densities, an elevated F peak altitude, and low electron and ion temperatures [*Foster*, 1993]. Phenomenologically, SED is primarily a feature of the post-noon sector at middle latitudes with significant elongation in longitude while TOI is more elongated in a latitudinal sense from middle to polar latitudes in the noon sector.

The source of plasma for the TOI has been a particular focus of study. *Foster et al.* [2005] presented a multi-instrument analysis of the polar TOI during a large geomagnetic storm and suggested the dayside source of the TOI was an SED plume transported from subauroral latitudes in the dusk sector by SAPS disturbance electric fields. The plume of enhanced total electron content (TEC) was seen to closely follow high latitude convection streamlines derived from SuperDARN and satellite observations, although the lower latitude

sunward convecting regions were missed in the SuperDARN coverage. *Hosokawa et al.* [2010] investigated the temporal evolution and spatial structure of a TOI driven by a coronal mass ejection (CME), finding that both positive storm effects and a buildup of source plasma in the mid-latitude ionosphere are necessary for the formation of a continuous polar TOI.

Results from other studies have suggested that an SED plume will not always give rise to a TOI. *Coster et al.* [2006] identified several storms when SED structures were produced but no TOI was observed to reach into the dayside cusp region. The strength and/or orientation of the interplanetary magnetic field (IMF) were suggested as possible factors controlling the formation of a TOI from SED.

The goals of this paper are to further understand the mechanisms responsible for the formation of TOI from SEDs and to determine why a TOI does not always occur when an SED is present. It is now possible to make continuous, direct observations of convection electric fields at mid-latitudes in the region where this generation of TOI from SED occurs. Recently constructed SuperDARN radars at mid-latitudes in North America overlook an increasingly dense network of GPS receivers capable of observing large-scale density structures such as SED and the mid-latitude trough [*Coster et al.*, 2003, 2007; *Basu et al.*, 2008]. New analysis tools developed at Virginia Tech allow for side-by-side comparisons of these two datasets on a global scale in a variety of formats. We present an analysis of CME-driven geomagnetic storm activity on 26-27 September 2011 that featured both TOI and SED features.

3.2 Datasets

3.2.1 SuperDARN HF Radars

The Super Dual Auroral Radar Network is an international network of high frequency (HF) coherent radars. SuperDARN radars operate continuously to measure line-of-sight

(LOS) velocities, backscattered power, and spectral width from decameter-scale plasma irregularities in the ionosphere [*Greenwald et al.*, 1985; *Chisham et al.*, 2007]. The measured $\mathbf{E}\times\mathbf{B}$ drift velocities of these plasma irregularities are routinely used to derive global electric field maps that describe the large-scale circulation of plasma in the ionosphere [*Ruohoniemi and Baker*, 1998]. The radars are frequency agile over a bandwidth of 8-20 MHz to allow for monitoring of different propagation modes and to follow changing ionospheric conditions. The standard scan mode consists of 16 beams separated in azimuth by 3.3° with sampling in 45 km range gates that begin at a distance of 180 km, creating a field of view that extends ∼52° in azimuth and several thousand km in range. A full scan typically allows for 1 or 2 minute resolution in this mode. Figure 3.1 shows the coverage available with SuperDARN as of July 2012 in both the northern and southern hemispheres.

In order to better map the expansion of the high-latitude convection pattern during periods of geomagnetic disturbance, the SuperDARN network has been expanding to mid-latitudes. The first two North American mid-latitude radars were constructed in Virginia at the NASA Wallops Space Flight Facility (2005) and on the grounds of the Virginia Tech Agricultural Research and Extension Center facility near Blackstone (2008). With the support of the NSF Mid-Sized Infrastructure Program, a chain of mid-latitude radars is under construction with twin-radar builds completed in Kansas (2009) and Oregon (2010). These mid-latitude radars have provided new opportunities to examine mid-latitude ionospheric electrodynamics with unprecedented spatial and temporal coverage [*Oksavik et al.*, 2006; *Baker et al.*, 2007]. Recently, *Clausen et al.* [2012] examined the time evolution and longitudinal velocity variations of a SAPS feature observed across North America while *Grocott et al.* [2011] and *Kunduri et al.* [2012] studied the magnetospheric dynamics and interhemispheric conjugacy of a SAPS event observed simultaneously in the northern and southern hemispheres.

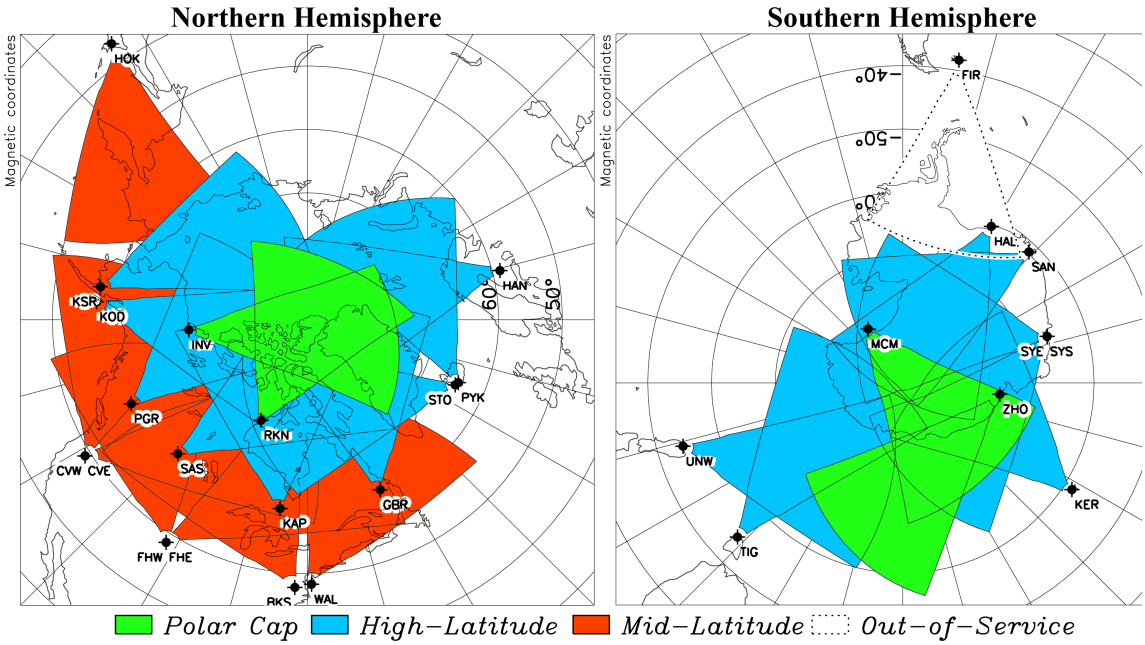

Figure 3.1: Fields of view of SuperDARN radars in northern (left) and southern (right) hemispheres as of July 2012. Mid-latitude, high-latitude, and polar radar FOVs are shaded red, blue, and green respectively.

The velocity measurements from the SuperDARN HF radars can be combined into a global map of ionospheric plasma convection using the technique described by *Ruohoniemi and Baker* [1998] and *Shepherd and Ruohoniemi* [2000]. Figure 3.2 shows the map obtained for the 19:30-19:32 UT interval on 26 September 2011. The contours of constant electrostatic potential constitute streamlines for F region plasma convection. The pattern is predominantly two-cell with a pronounced dayside "throat" feature that can be expected to channel plasma into the polar cap from lower latitudes. Velocity vectors are drawn where velocity data were available from the radars; additional data were provided by a statistical model that is keyed to the prevailing IMF conditions. The coverage by the radars is extensive over North America and provides strong constraints for the fitted pattern; in particular, for the convergence of flows on the dayside that defines the throat. For this study the convection pattern has been generated at a cadence of two minutes. In addition, we present plots of "raw" LOS velocity data from a subset of the SuperDARN radars that overlook the dayside

throat feature. These will serve to show the extent of the areas of HF backscattering as well as the directly measured plasma drift velocities. The occurrence of backscatter for the SuperDARN HF radars indicates the presence of small-scale (∼10 m) irregularities in the ionospheric plasma.

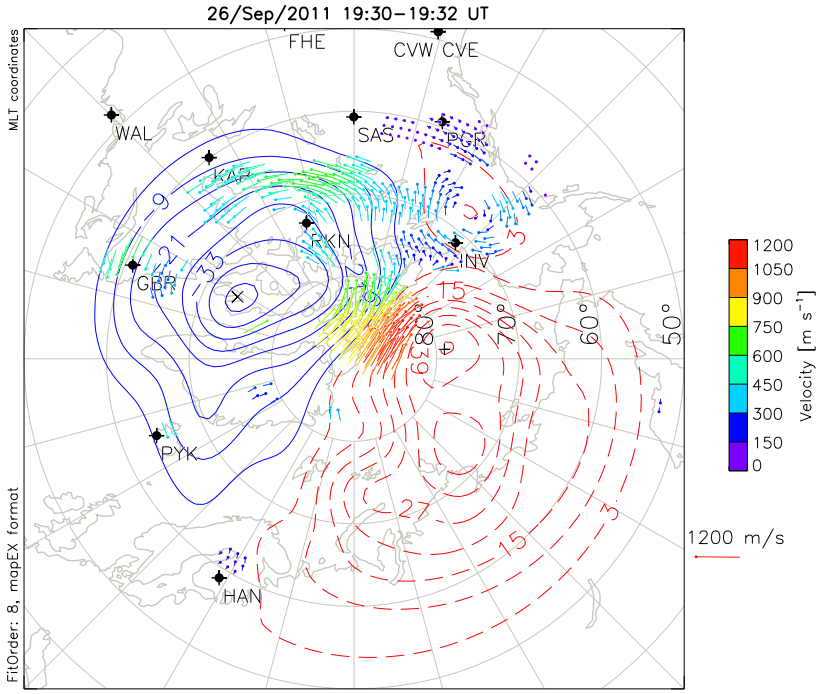

Figure 3.2: Map of plasma convection obtained for 26 September 2011, 19:30 - 19:32 UT, using the standard SuperDARN fitting technique as described in the text and plotted in magnetic local time versus magnetic latitude with magnetic noon at the top. The contours indicate lines of constant electrostatic potential; the contour step is 6 kV and solid/dashed contours indicate negative/positive signs on the potential. The positions and 3-letter names of the radars contributing to the solution are indicated.

3.2.2 GPS Total Electron Content

Maps of total electron content (TEC) are commonly used to depict the highly variable nature of the Earth's ionosphere. Researchers at MIT Haystack Observatory generate maps of vertically integrated TEC from a global network of GPS receivers and offer their data product to the larger scientific community via the Madrigal database [*Rideout and Coster*,

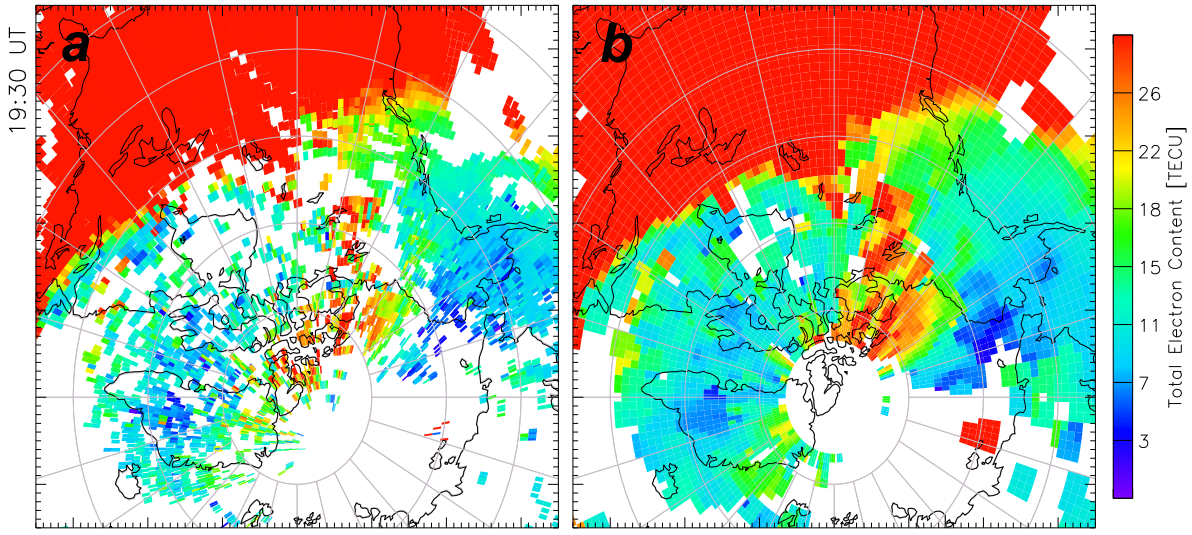

Figure 3.3: (a) Three 5-minute maps of GPS TEC observations overlaid on top of one another from 19:25-19:40 UT, after mapping to MLT-MLAT coordinates. (b) Median-filtered GPS TEC data spanning the same interval, centered at 19:30 UT. No TEC data are plotted above $\Lambda = 85°$ due to difficulties in spatial filtering over the polar cap. Figures are plotted with magnetic noon at the top and midnight at the bottom.

2006]. The TEC measurements of the ionosphere describe the total number of electrons contained in a cylinder of cross-sectional area 1 m^2 that extends vertically above a given point on the Earth and extends all the way through the ionosphere. One TEC unit (TECU) is given as $1{\times}10^{16}$ electrons/m^2; typical peak dayside values can range from less than 10 TECU on a quiet day to the hundreds of TECU observed during strong geomagnetic storm activity. Measurements are binned into 1° by 1° cells at 5-minute resolution.

Figure 3.3a shows three consecutive 5-minute GPS TEC maps from 19:25-19:40 UT overlaid on top of one another after mapping to MLT-MLAT coordinates. Using a standard spatiotemporal median filtering technique, observations derived at MIT Haystack Observatory from the three intervals are used to generate the single TEC map for 19:30 UT seen in Figure 3.3b. It is important to note that as a result of the filtering technique no TEC measurements above 85°Λ are included due to difficulties comparing adjacent cells near the pole. The SuperDARN convection pattern from Figure 3.2 can be overlaid onto the filtered TEC

map, as shown in Figure 3.4a. This reveals that the dayside TEC enhancements that extend from mid-latitudes into the polar cap ($\Lambda > 80°$) are substantially ordered by the pattern of convection streamlines. Regions of plasma entrained by high-speed convection flow are indicated by the close spacing of contour lines rather than the pattern's equatorward extent. Figure 3.4b offers a view of the spatial distribution of radar backscatter and the LOS velocity measurements that were available from a subset of the SuperDARN radars. The spatial correspondence especially at higher latitudes are suggestive that the TEC enhancement regions were associated with the small-scale irregularities responsible for HF coherent backscatter. A nonlinear color scale has been used for the LOS velocities to better observe variability in the low-velocity flows seen at mid-latitudes in addition to the high-velocity motion across the polar cap.

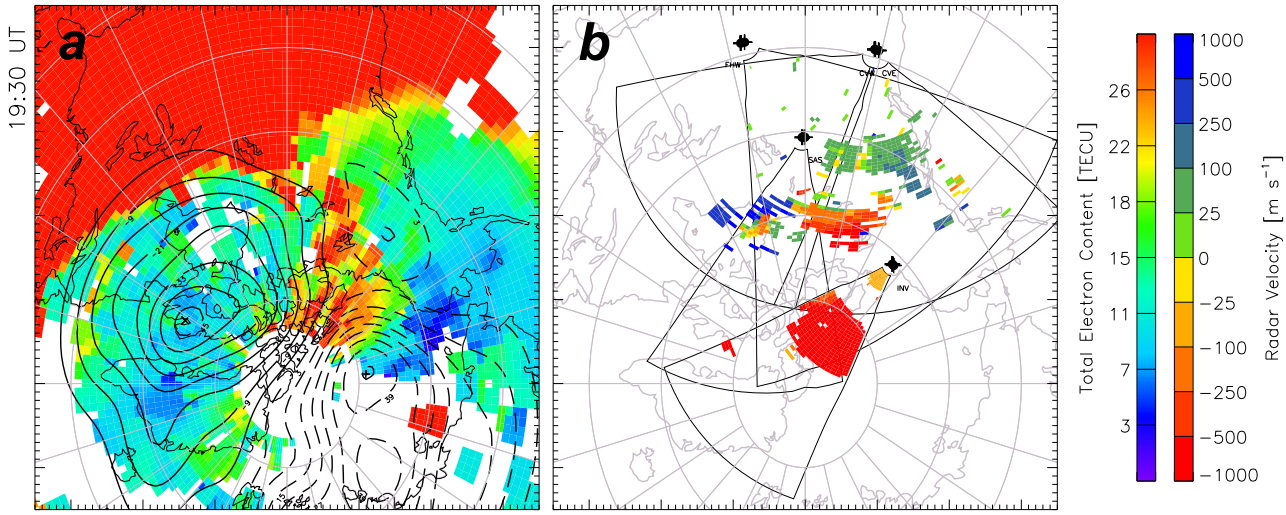

Figure 3.4: (a) GPS TEC map with SuperDARN convectin pattern overlaid and (b) line-of-sight (LOS) velocity measurements from selected SuperDARN radars with fields of view indicated, again plotted with magnetic noon at the top.

3.2.3 Online Plotting Tools

The plotting tools applied in this study are available online at the Space@VT SuperDARN website (http://vt.superdarn.org). Using GPS data downloaded from the Madrigal database, users are able to perform spatial/temporal median filtering of the TEC data, turn on and off radar measurements, overlay convection patterns, select from different coordinate systems, and choose the hemisphere to be displayed. Options are also available to plot measurements for a single 5 minute period or as an animation over a user-defined interval. Source code and documentation for the use of the plotting tools are freely available on the website.

3.3 Observations

3.3.1 Event Overview

In this paper, we examine the formation of a polar TOI from mid-latitude SED during a CME-driven geomagnetic storm on 26-27 September 2011. Solar interplanetary magnetic field (IMF) has been demonstrated to strongly affect the features of SEDs and TOIs [*Foster et al.*, 2005; *Hosokawa et al.*, 2010]. Figure 3.5 shows geomagnetic indices and solar wind parameters for a 16 hour period during this event. The arrival of the CME at the Earth's magnetosphere is seen in the top panel at 12:40 UT as an abrupt intensification followed by a steady decline from +50 to -100 nT in the Sym-H index, which is a proxy for the strength of the symmetric part of the ring current.

We have surveyed the timeline of SED and TOI occurrence in the TEC data and determined that a linked SED/TOI event occurred between 18:30-19:40 UT and that a second SED period lacked an accompanying TOI in the 20:30-00:30 UT interval. These periods are

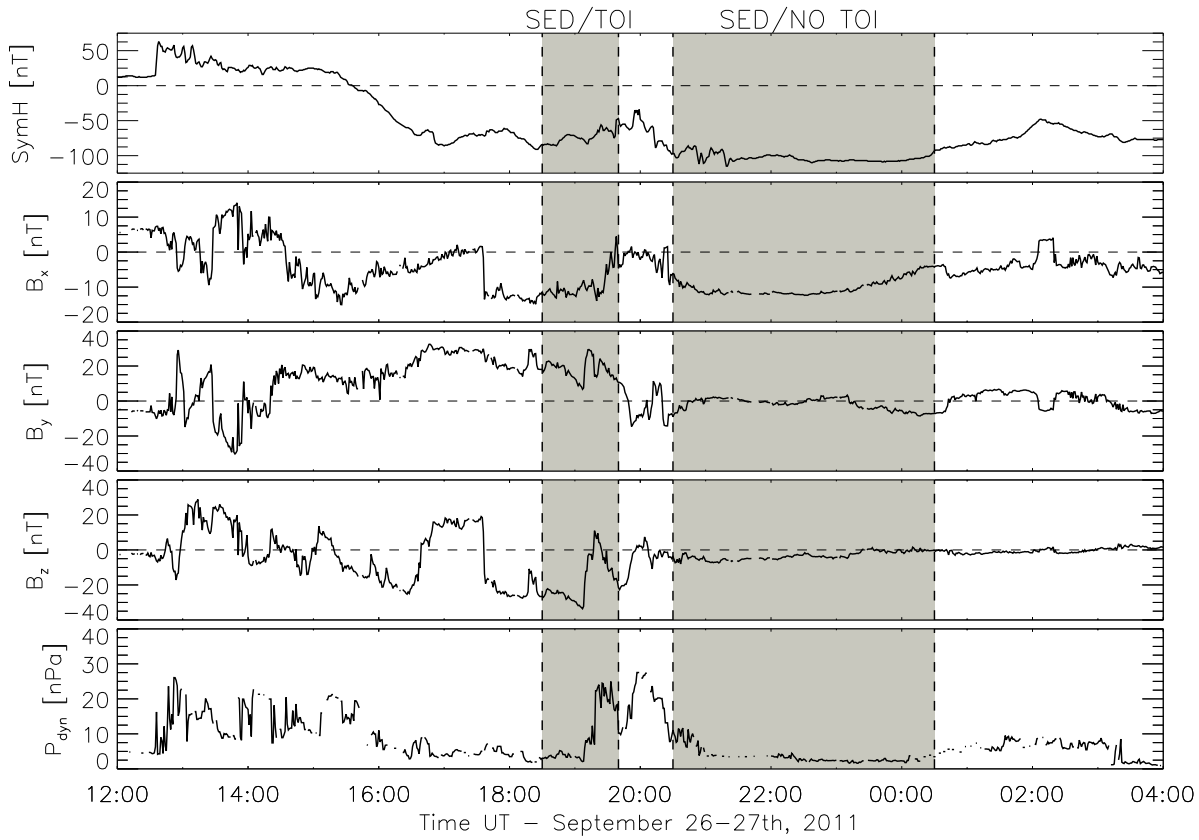

Figure 3.5: Geomagnetic and solar wind OMNI parameters on 26-27 September 2011 (from top): Sym-H index, OMNI IMF Bx, By, Bz, and dynamic pressure. The first shaded region indicates the interval from 18:30-19:40 UT when a TOI formed from mid-latitude SED as identified from GPS TEC maps (SED/TOI). The second shaded region indicates a later period from 20:30-00:30 UT when no TOI was observed forming from mid-latitude SED (SED/NO TOI).

highlighted in Figure 3.5 and clearly fall into the storm main phase.

The next three panels in Figure 3.5 show the IMF Bx, By, and Bz components from the OMNI 2 database [*King and Papitashvili*, 2006]. The interval when a TOI was observed (first shaded region) is characterized by sustained positive IMF By and a strong southward IMF (< -20 nT) until the northward turning at 19:15 UT. Coincident with this northward Bz turning is an increase in solar wind dynamic pressure from nearly zero to 25 nPa (bottom panel). Thirty minutes later at 20:00 UT, a second and final northward Bz turning is also accompanied by a sudden increase in dynamic pressure. After the TOI had subsided and only an SED plume remained (second shaded region), the IMF By and Bz components remained fairly constant and low in magnitude. The positive By and southward Bz components of the IMF from 17:30-19:20 UT meet the conditions described by *Hosokawa et al.* [2010] for the formation of a continuous polar TOI. As we shall see, the large transitions in Bz during the early part of the storm controlled the evolution of the SED and emergence of TOI.

3.3.2 Formation of TOI

Following the southward turning of the IMF at 17:37 UT on 26 September 2011 (Figure 3.5), an SED plume began to form over eastern North America. Figure 3.6 shows the TEC distribution in the Northern Hemisphere before and just after the southward turning. At 17:30 UT, the mid-latitude plasma densities appear fairly uniform in magnitude on the dayside (Figure 3.6a). Thirty minutes later at 18:00 UT, a new region of enhanced TEC corresponding to an SED plume is emerging at middle latitudes in the afternoon sector (Figure 3.6b). Note that we have increased the TEC color scale from that applied in Figure 3.3 and Figure 3.4 in order to show the SED feature more prominently.

A continuous polar TOI was observed to form from mid-latitude SED in GPS TEC

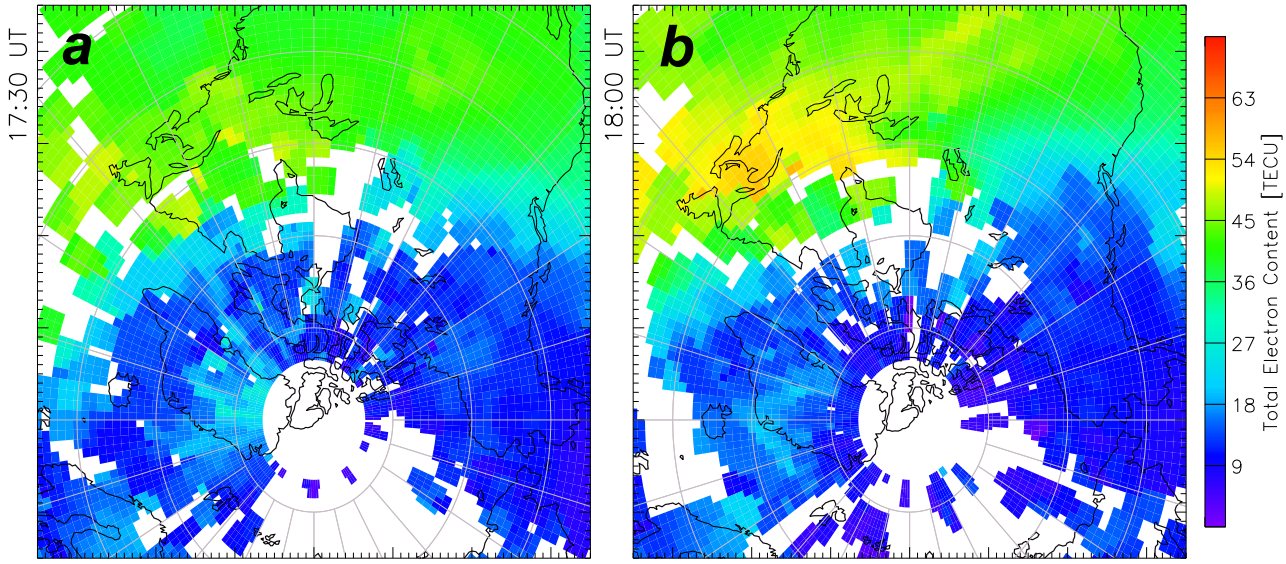

Figure 3.6: GPS TEC maps showing the development of an SED plume over North America at (a) 17:30 UT and (b) 18:00 UT on 26 September 2011. The color scale has been increased from Figure 3.3 and Figure 3.4 to highlight the region of enhanced TEC corresponding to the SED plume in (b). Figures are plotted with magnetic noon at the top.

measurements from 18:30-19:40 UT. Figure 3.7 shows the time evolution of the TOI, ionospheric convection, and HF backscatter patches as seen by GPS TEC and SuperDARN. A channel of enhanced TEC is seen progressing poleward from a mid-latitude SED feature by 18:30 UT and entering the polar cap by 19:30 UT. Similar to the results presented by *Foster et al.* [2005], the channel of enhanced TEC closely follows the streamlines of convection independently derived from the global network of SuperDARN radars. Sustained positive IMF By lasting until 19:50 UT is responsible for the clockwise rotation of the global convection pattern, bringing the dusk cell onto the dayside. When combined with the strongly southward IMF, this allows for the enhanced dusk convection cell to transport dense mid-latitude ionospheric plasma into the throat feature as seen in Figure 3.7b.

The plasma within the TOI is convected across the pole at speeds in excess of 1 km/s. The continuous TOI persists until just after 19:30 UT, when the base of the TOI detaches from its source region at middle latitudes. Changes in the IMF conditions alter the convection

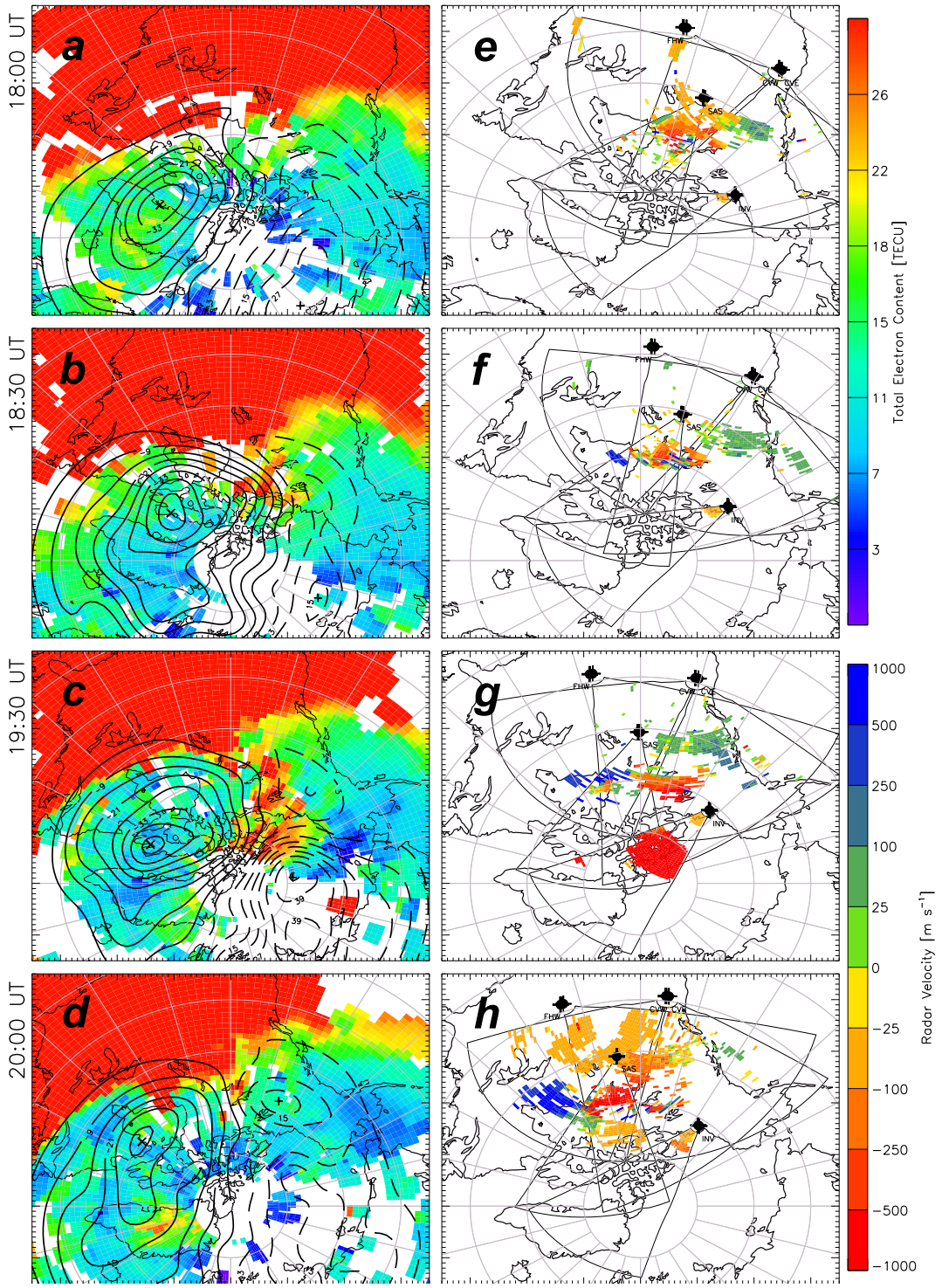

Figure 3.7: (a-d) GPS TEC maps depicting evolution of a polar tongue of ionization (TOI) with SuperDARN convection patterns overlaid. (e-h) SuperDARN LOS velocity measurements from ionospheric scatter for selected radars. Figures are plotted in magnetic local time with magnetic noon at the top for times 18:00, 18:30, 19:30, and 20:00 UT.

pattern such that more of the plasma flow in the throat is associated with the dawn cell, which lacks a connection to a high-density reservoir of plasma. The SuperDARN velocity plots on the right hand side of Figure 3.7 show regions of HF backscatter due to small-scale irregularities and the accompanying LOS plasma velocity. Although many factors influence the occurrence of the HF backscatter, there are indications that the TOI is a source of backscatter [*Hosokawa et al.*, 2009]. In particular, by 19:30 UT an irregularity backscatter patch has formed in the polar cap that is spatially coincident with the extension of the TOI, suggesting small-scale irregularity formation. Figure 3.7d indicates that by 20:00 UT the large continuous patch of plasma has broken up into smaller patches that have begun to exit the polar cap and become entrained in the dusk convection cell. A movie of GPS TEC maps showing the evolution of SED/TOI activity is available in the online auxiliary materials.

3.3.3 Storm Enhanced Density

A plume of enhanced TEC is observed some time after the disappearance of the TOI (Figure 3.8a-d). One endpoint of the SED plume is attached to the dense source plasma at middle latitudes in the afternoon sector while the other remains fixed in magnetic latitude/local time near the dayside cusp. As the mid-latitude region of enhanced TEC corotates with the Earth away from noon, the plume elongates in magnetic local time at a near-constant latitude and lasts until approximately 00:30 UT on 27 September 2011. The backscatter observed by the SuperDARN radars remains poleward of this region throughout its duration (Figure 3.8e-h). This implies that, unlike the earlier TOI formed from an SED, this plume was not the seat of active irregularity formation. While IMF Bz was still negative during this period (Figure 3.5), it was greatly reduced in magnitude from the earlier SED/TOI interval and IMF By was near zero. (Although the Bx component was substantial, its impact on convection during equinoctial periods is thought to be minimal). As a result

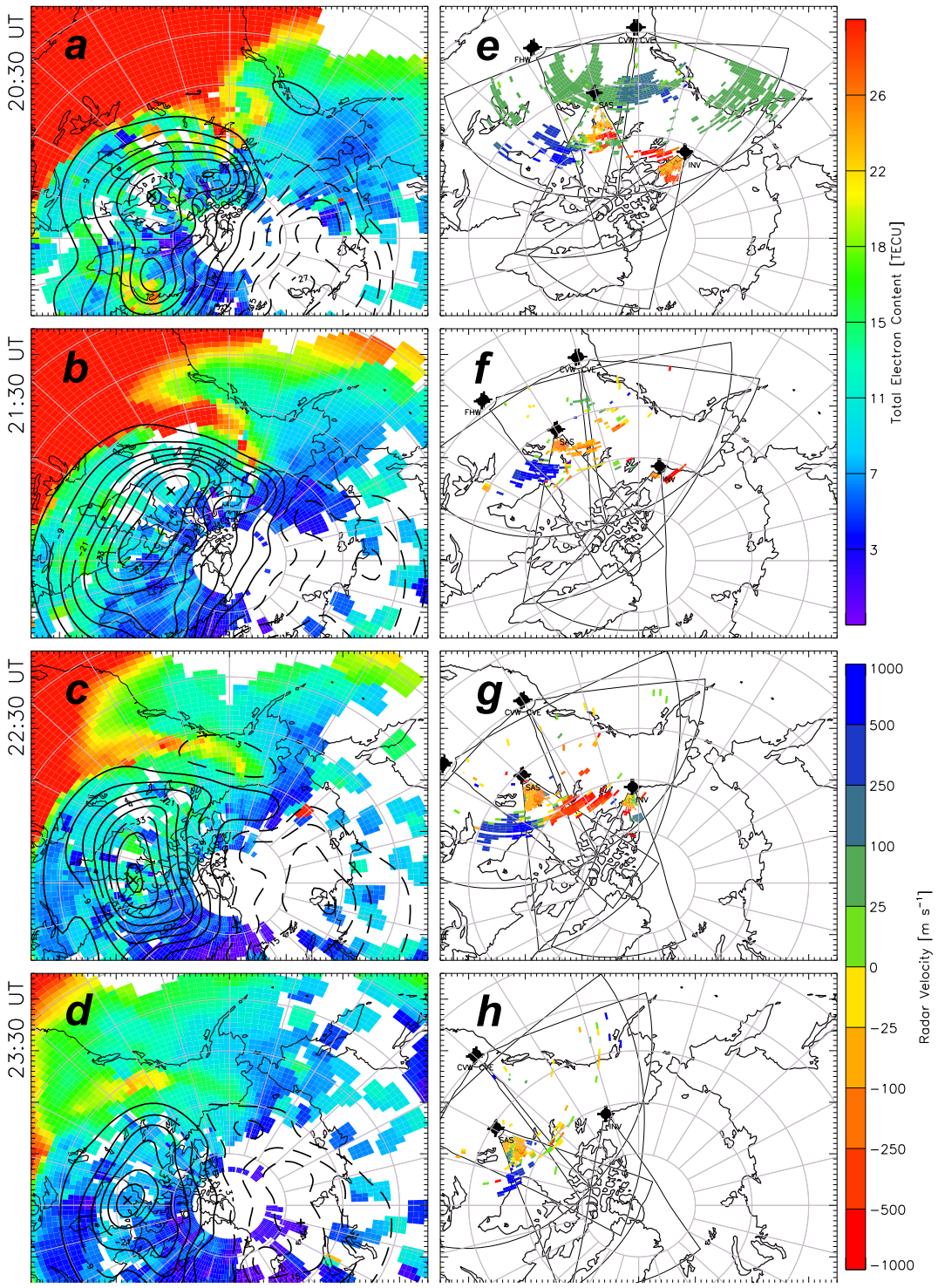

Figure 3.8: In the same format as Figure 3.7, (a-d) GPS TEC maps depicting evolution of "fossil" storm enhanced density (SED), and (e-h) radar velocity measurements for times 20:30, 21:30, 22:30, and 23:30 UT.

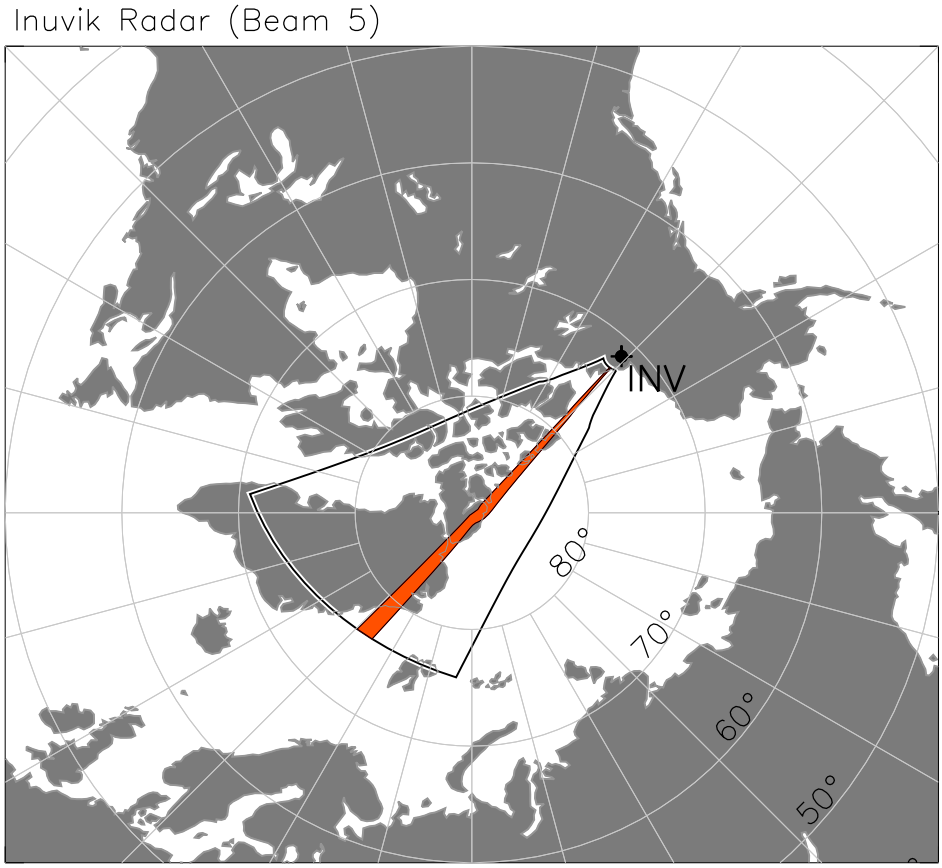

Figure 3.9: Field of view of Inuvik radar with beam 5 highlighted, plotted with magnetic noon at the top of the figure for 19:30 UT. This beam looks into the polar cap and is aligned with the throat of the TOI feature described in the text.

the convection electric fields did not extent to lower latitudes such that mid-latitude ionospheric plasma was entrained to flow into the polar cap. This is apparent from weakening of the convection pattern and the distinct poleward retreat of the lowest convection contour from the enhanced TEC region. This plume was consequently unproductive in terms of TOI and small-scale irregularity formation, and persisted rather as a "fossil" feature within the plasma distribution.

We examine GPS TEC and SuperDARN data along a selected radar beam to gain further insight into the degree of spatial coincidence of the density enhancements and backscatter from small-scale irregularities. The Inuvik radar is situated at a very high latitude

($\Lambda = 71.5°$) and looks deep into the polar cap as shown in Figure 3.9. Figure 3.10 shows backscattered power, LOS Doppler velocity, and nearest GPS TEC data along beam 5 of the Inuvik SuperDARN radar as a function of slant range (distance travelled by a transmitted signal through the ionosphere to a backscattering irregularity). The two intervals of SED activity previously indicated in Figure 3.5 are again highlighted in each of the panels. The plot of backscattered power indicates a sequence of poleward propagating HF backscatter patches were observed in the latter part of the first interval. These were associated with very high velocities away from the radar (antisunward), at the same time as the region of enhanced TEC passed through the radar FOV over the polar cap. Thus the TOI was productive of small-scale irregularities within patchy-like features. No sign of the later "fossil" SED seen in Figure 3.8c is observed in either the radar or TEC polar cap measurements, indicating that the high-TEC plasma was no longer being convected to high latitudes. (An earlier TOI at 16:30 UT can be seen entering the radar FOV in Figure 3.10c, although the lower velocities and shorter duration observed by the radar suggest a weaker event.)

3.4 Discussion

We have presented observations of the formation of a polar TOI during a geomagnetic storm on 26-27 September 2011 using GPS TEC and SuperDARN measurements. Early in the event the high-latitude convection electric fields expanded equatorward to middle latitudes, encountering a region of enhanced plasma and entraining the flow of dense F region plasma through the dayside cusp and across the polar cap at velocities in excess of 1400 m/s. This scenario has been postulated previously by *Foster et al.* [2005] and *Hosokawa et al.* [2010]. Here, for the first time simultaneous measurements of GPS TEC and SuperDARN ionospheric convection at mid-latitudes have been available to confirm the equatorward expansion of the high-latitude convection electric fields into the dense source

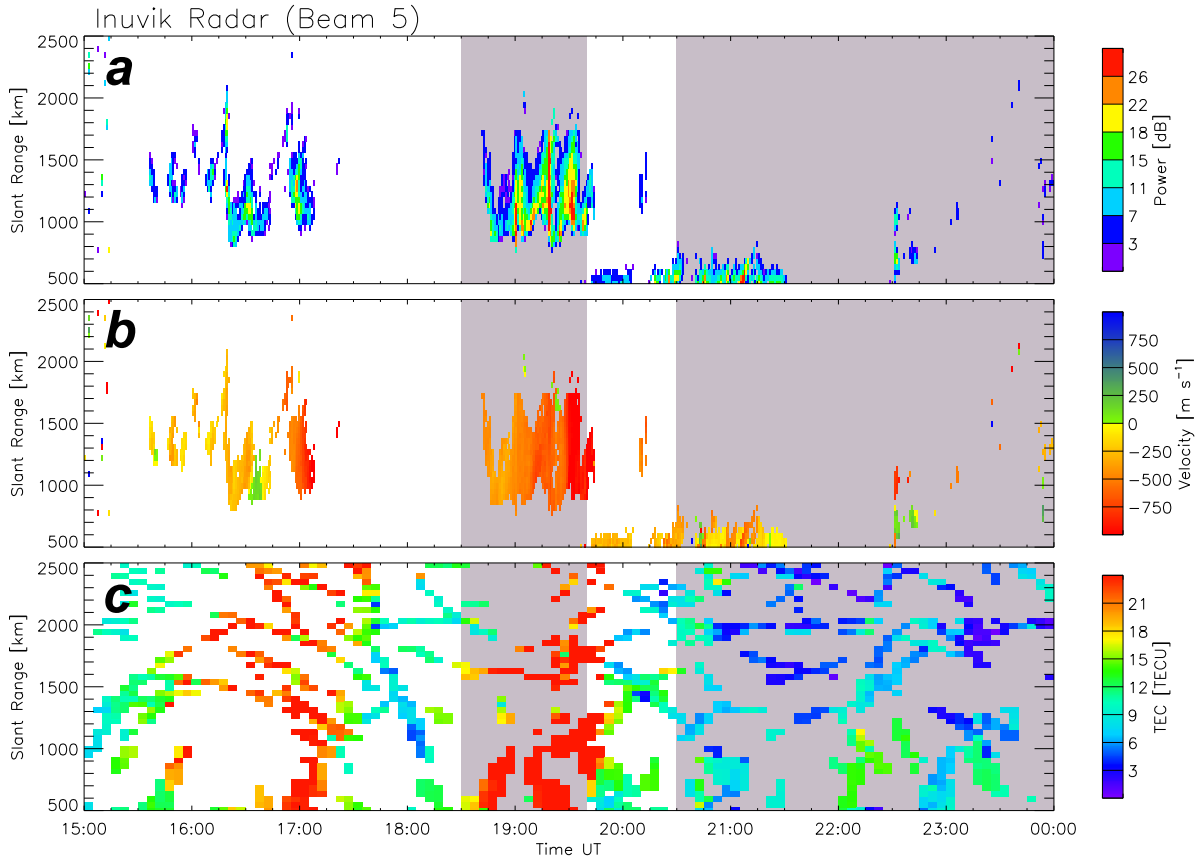

Figure 3.10: (a) The backscattered power and (b) LOS Doppler velocity data from beam 5 of the polar Inuvik radar in range-time-intensity (RTI) format. (c) GPS TEC data closest to each range cell along the same beam. In the same manner as Figure 3.5, the two intervals of SED activity as observed from GPS TEC maps are shaded.

region and the poleward retreat of the convection pattern which strands the resulting fossil SED at subauroral latitudes. It is also shown that the TEC enhancements that map out the TOI are associated with small-scale irregularities responsible for HF backscatter.

The fossil SED observed from 20:30-00:30 UT has many features similar to the event described by *Coster et al.* [2006] which did not form a TOI despite the plume of enhanced TEC reaching the dayside cusp region. For the 26-27 September 2011 event, during the inactive SED period IMF conditions returned to a quiet state with both the By and Bz components nearly zero (Figure 3.5). No ionospheric backscatter was observed by SuperDARN radars within the region of enhanced TEC that persisted, suggesting the disappearance of the drivers responsible for small-scale irregularity formation. This inactive persistence is very similar to the fossil ionospheric trough described by *Evans et al.* [1983], whereby an ionospheric perturbation formed by an active storm process will persist in the absence of daylight as it co-rotates through the night sector at a near-constant latitude. This phenomenon has also been discussed in relation to subauroral ion drifts (now known as SAPS) and stable auroral red (SAR) arcs by *Anderson et al.* [1991] and *Foster et al.* [1994]. The later SED plume (Figure 3.8) is in effect a remnant of the earlier activity and akin to a "fossil" SED feature. By contrast, the earlier SED encountered strong electric fields and produced a TOI.

We conclude our discussion by summarizing the SED/TOI activity through the two intervals in terms of magnetic reconnection. When the IMF Bz component turned strongly southward, enhanced dayside reconnection results in plasma that was previously on closed field lines at lower latitudes being subsequently on open field lines. This leads to the excitation of convection electric fields as the newly open flux evolves over the magnetopause, thus drawing plasma from the closed-field line regime (where the SED is located) into the polar cap (producing the TOI). When IMF Bz experiences a northward turning, dayside reconnection stalls and there is no longer a mechanism by which plasma can move from the

closed to the open field line regime [*Cowley and Lockwood*, 1996]. Hence the SED plume stagnates as a fossil feature and no TOI is produced.

3.5 Summary

In this paper, we have examined the relationship of convection electric fields to the formation of a polar cap tongue of ionization (TOI) from mid-latitude plumes of storm enhanced density (SED). Observations from the geomagnetic storm on 26-27 September 2011 were presented for two cases of potential TOI formation from an SED. During an hours-long period of dynamic geomagnetic activity, a channel of high density F region plasma was transported from the dayside mid-latitude ionosphere and into the polar cap by enhanced convection electric fields extending to middle latitudes ($\Lambda = 60°$). The TEC enhancements that mapped out the TOI were associated with HF backscatter, indicating that the TOI is the seat of active formation of small-scale irregularities. After the solar wind IMF conditions quieted and the dayside convection electric fields retreated to higher latitudes ($\Lambda \geq 70°$), an SED was observed extending to, but not entering, the dayside cusp region. This high-TEC feature persisted at a near-constant latitude for several hours and elongated in magnetic local time as the initial furthest dayside extent co-rotated with the Earth. No ionospheric scatter from the SuperDARN radars was observed within this remnant SED region. For this fossil feature, the source mechanism (enhanced electric fields) previously drawing the plasma from mid-latitudes and into the polar cap was no longer locally active. Thus we have demonstrated the controlling role exercised by the convection electric field in generating a TOI from mid-latitude SED.

Acknowledgments

The authors from Virginia Tech thank the National Science Foundation for support under grants AGS-0946900 and AGS-0838219. The authors from MIT Haystack also thank the National Science Foundation for support under grant ATM-0856093. EGT acknowledges support provided by the Virginia Space Grant Consortium under a graduate research fellowship. LBNC acknowledges funding from the Deutsches Zentrum fuer Luft- and Raumfahrt under grant 50OC1102 and 50OC1001. Sym-H indices were obtained from the World Data Center in Kyoto. The OMNI data were obtained from the GSFC/SPDF OMNIWeb interface at http://omniweb.gsfc.nasa.gov. The TEC data were downloaded through the Madrigal database at Haystack Observatory. The authors acknowledge the use of SuperDARN data. SuperDARN data is a collection of radars funded by national scientific funding agencies of Australia, Canada, China, France, Japan, South Africa, United Kingdom, and United States of America.

Chapter 4

Active remote sensing of sea ice cover using SuperDARN HF radars

4.1 Introduction

In addition to field-aligned plasma irregularities in the ionosphere, SuperDARN radars also observe backscatter from Earth's surface on a daily basis. Scientists have used these reflections from the Earth's surface to characterize the ionosphere in variety of ways, such as monitoring atmospheric gravity waves, E and F layer critical frequencies, and ultra-low frequency (ULF) wave propagation [*André et al.*, 1998]. Assuming the Earth's surface is homogenous, we expect ground scatter to be fairly uniformly distributed in azimuth (beam). The range interval is determined by local ionospheric properties, such as electron densities and peak altitude. Variations in ground scatter observations with azimuth suggest effects from the underlying surface rather than the ionosphere. To demonstrate this concept, Figure 4.1 shows ray-tracing results for expected ground scatter observed by the Goose Bay radar using a model ionosphere at 15:00 UT on October 15, 2000 [*de Larquier et al.*, 2011]. The relative backscattered power from the ground varies as a function of range rather than azimuth because only ionospheric effects are considered.

Relatively few scientific papers have attempted to study these ground surface effects on backscattered observations [*Shand et al.*, 1998; *Ponomarenko et al.*, 2010]. There has

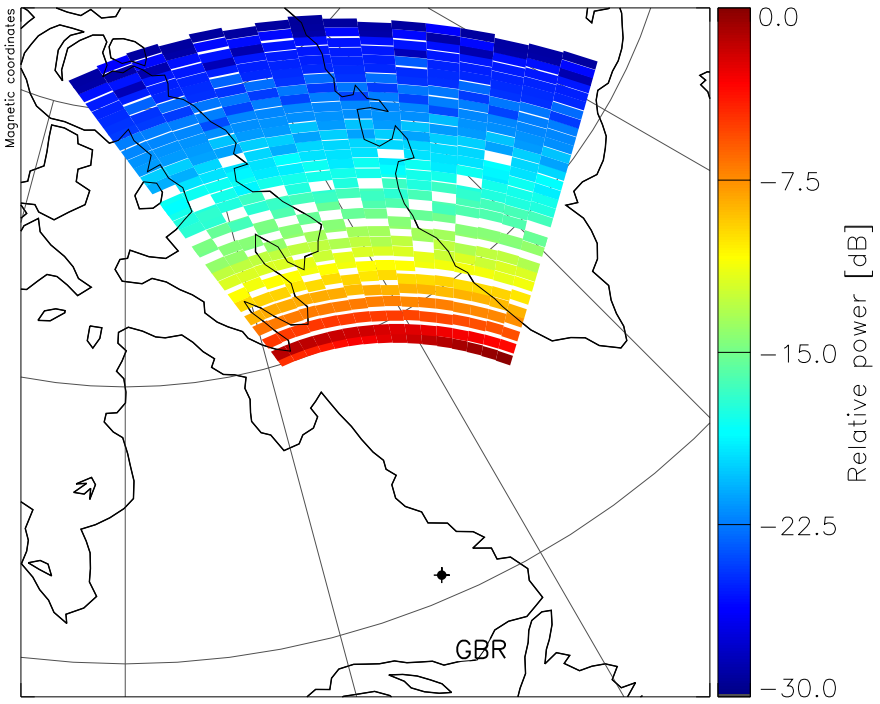

Figure 4.1: Ray-tracing results for predicted ground scatter for Goose Bay radar at 15:00 UT on October 15, 2000. The 2011 International Reference Ionosphere (IRI-2011) model is used to simulate ionospheric parameters.

also been a recent attempt to characterize ocean waves by *Greenwood et al.* [2011] using the pair of southern hemisphere TIGER SuperDARN radars. In this chapter we discuss this previous work as well as demonstrate new results from comparing statistical monthly radar ground scatter occurrence rates to sea ice boundaries independently derived from satellite observations for two purposes. First, we wish to improve the accuracy of current SuperDARN ray-tracing models by including ground surface effects. Our second goal is to test the ability of SuperDARN radars to quantify sea surface roughness for eventual comparison with altimeter measurements.

The first discussion of ground surface effects on SuperDARN observations found in the literature was presented by *Shand et al.* [1998]. This work was concerned with studying dynamics of the Greenland glacier tongue (Odden) using ground scatter measurements from

the Pykkvibaer SuperDARN radar in Iceland. The location of the sea ice boundary was found using the passive Special Sensor Microwave/Imagers (SSM/I) onboard the Defense Meteorological Satellite Program (DMSP) spacecraft. In Figure 4.2, the Odden ice tongue can be seen forming off the east coast of Greenland on November 7, 1996 as a small, circular null in ground scatter surrounded by a region of strong backscatter occurrence coming from the surrounding ocean. Seventeen days later on November 24, the size of the glacier tongue had increased with blank patches within the body of the tongue marking normalized ground scatter percentages below 40%. In the next frame on November 28, these blank patches of low ground scatter occurrence have grown to cover a larger portion of the ice tongue. By December 10, 1996 the ice tongue had entirely detached from the Greenland coast and began to drift away into the open ocean. In each of these frames the presence of sea ice has altered the radar scattering mechanisms over the regions where little or no radar ground scatter is observed, resulting in a loss of returns. This was the last published effort to analyze SuperDARN ground backscatter to resolve surface effects for over a decade.

Ponomarenko et al. [2010] studied the characteristics of SuperDARN ground scatter as observed by the Rankin Inlet radar located at polar latitudes. Using relief maps and satellite measurements of the extent of sea ice cover, they demonstrated that ice sheets rarely produced detectable backscatter, mountain ranges are the major source of ground scatter as they produce echoes at all seasons of the year, and sea surface becomes a significant source of ground scatter once the Arctic sea ice melts away. In this study, ground scatter echoes with signal-to-noise ratio (backscattered power) ≥ 6.0 across all hours of the day were considered. Figure 4.3 shows the seasonal variation in ground scatter occurrence and sea ice cover (gray shading) for March, June, September, and December 2008 within the Rankin Inlet radar FOV. The maximum ground scatter occurrence rate is seen at closer ranges in June compared to March and September, demonstrating the seasonal changes in

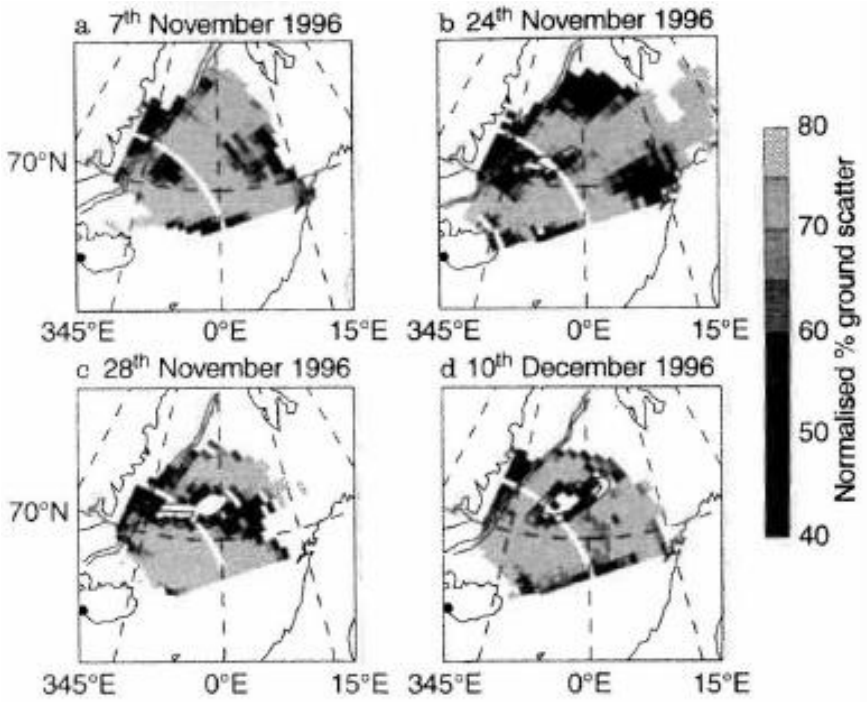

Figure 4.2: Daily average ground scatter observed by the Pykkvibaer radar in the region of Odden ice tongue. Solid lines represent approximate position of the 30% and 60% sea ice concentration boundaries determined from DMSP satellite imagery [*Shand et al.*, 1998].

propagation conditions. Regions of increased ground scatter are colocated with mountainous areas of Ellesmere, Devon, and Baffin Islands and the coastal areas of Greenland, while a significant decrease is within the sea ice cover boundaries.

For this study we build upon the previous efforts by *Shand et al.* [1998] and *Ponomarenko et al.* [2010] to analyze the variations in ground scatter observed by SuperDARN radars due to geographical surface effects. Where *Ponomarenko et al.* [2010] focused on only one polar cap radar, we consider two pairs of high-latitude radars with overlapping fields of view (FOVs). As mentioned in Section 1.2, SuperDARN radars cover a large portion of the Earth's surface at high latitudes where Arctic sea ice enters many of the radars' FOVs. An example of actual ground backscatter observed during a single scan from the Goose Bay radar at 15:00 UT on October 15, 2000 can be seen in Figure 4.4. Compared to the model ray-tracing results in

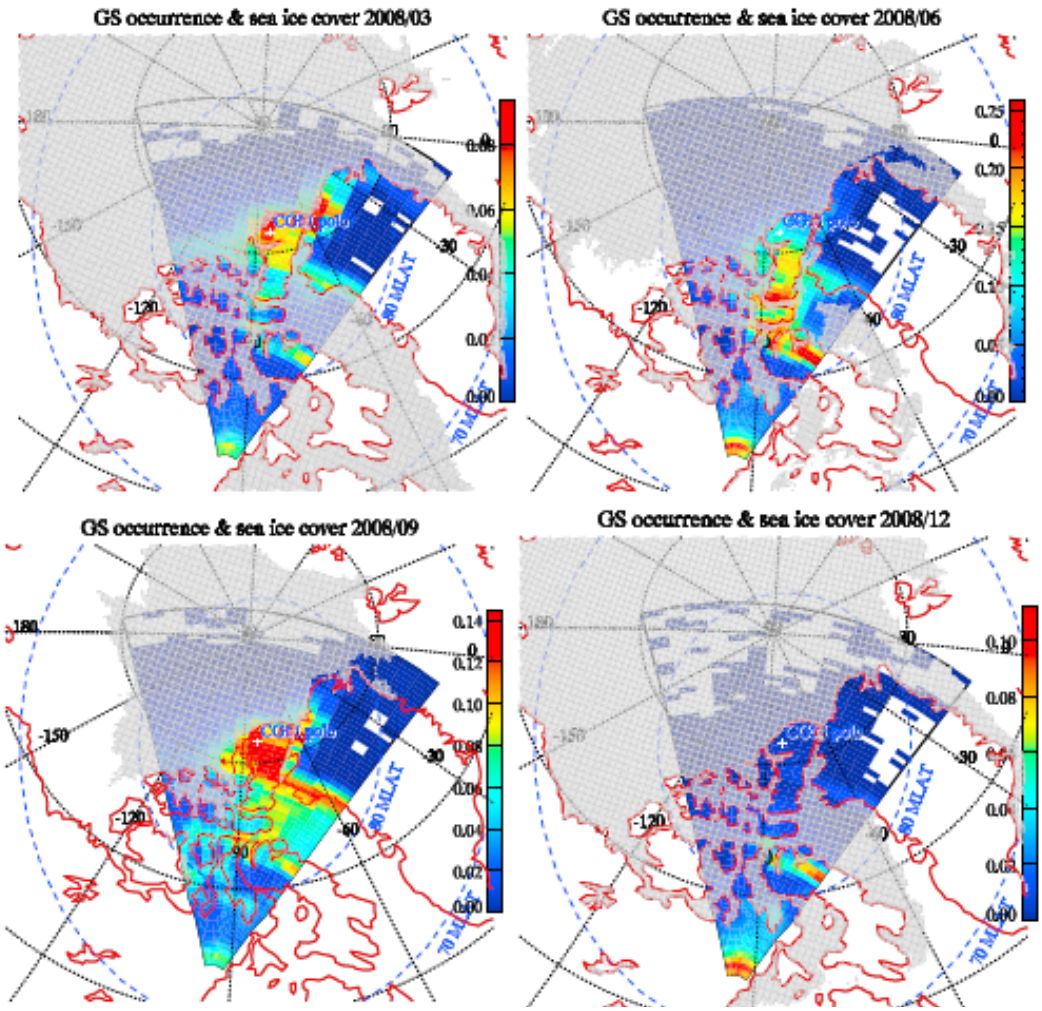

Figure 4.3: Seasonal variation in Rankin Inlet ground scatter occurrence and sea ice cover (gray shading) for March, June, September, and December 2008 [*Ponomarenko et al.*, 2010].

Figure 4.1, there is a noticeable decrease in the amount of ground scatter over Greenland and Baffin Island. A region of backscatter corresponding to the coastline on the opposite side of Greenland is seen in the right-most beams during this scan. Ground scatter mapped over the interior of Greenland is likely due to broadening of the radar phased array antenna beam when steering far from boresite.

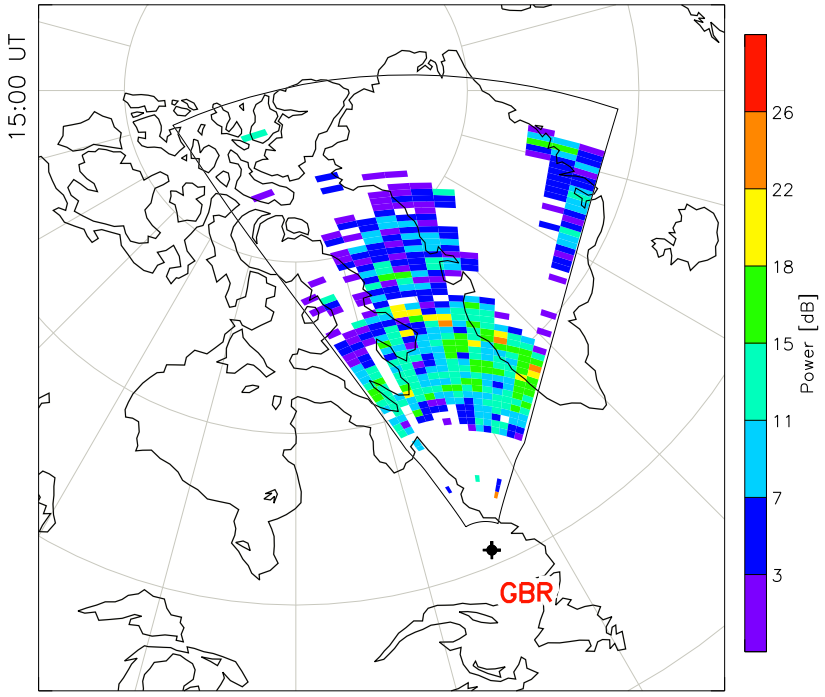

Figure 4.4: Field of view/scan plot of Goose Bay ground scatter power measurements for a single scan on October 15, 2000 at 15:00 UT.

4.2 Methodology

In this study, ground scatter occurrence rates have been calculated for four high-latitude radars overlooking the Hudson Bay and Davis Strait: Goose Bay, Stokkseyri, Saskatoon, and Kapuskasing. Using a similar method as *Ponomarenko et al.* [2010], ground scatter has been identified using the following criteria: 1. signal-to-noise ratio (backscattered power) $\geq$ 6.0 dB, and 2. the standard ground scatter flag (narrow spectral width, low Doppler velocity). Only the hours 11:00-17:00 local time have been considered in order to maximize the amount of ground scatter observed while reducing the possibility of mixed ground/ionospheric returns. In each frame the color scales are normalized to the maximum monthly occurrence. The first five range gates have been ignored when selecting the maximum monthly occurrence to avoid contamination from meteor scatter returns.

For comparison with sea ice boundaries, 24 km resolution sea ice data from the National Snow and Ice Data Center in Boulder, Colorado has been shaded on each of the figures. This data product comes from the Interactive Multisensor Snow and Ice Mapping System (IMS), which is manually determined by a satellite analyst. The primary image sources come from the NOAA Polar Operational Environment Satellites (POES) and is then supplemented by data from geostationary spacecraft including the Geostationary Operational Environment Satellites (GOES), Geostationary Meteorological Satellite (GMS), and the European Weather Satellite (METEOSAT). Ground-based observations and microwave imagers onboard DMSP satellites are also used for regions obstructed by cloud cover [*Fetterer and Webster*, 2011].

4.3 Results

The following four subsections show the calculated ground scatter occurrence rates for each of the four SuperDARN radars as described in Section 4.2. Similar to the results discused by *Ponomarenko et al.* [2010], the location of the strong bands of ground scatter are seen at closer range gates during winter months and farther range gates during summer months. In Figure 4.5, the Arctic sea ice can be seen advancing towards the Goose Bay radar during the fall and winter months (October - December, January - February). When the Davis Strait is uncovered by sea ice, the waters between Baffin Island and Greenland are the most productive source of ground backscatter. Once the Davis Strait is fully covered by sea ice in February/March, the brightest regions of ground scatter occurrence over the southern tip of Baffin Island and the western Greenland coast are split by the sea ice. As summer approaches and ionospheric conditions push the ground scatter band to further ranges, noticeable bite-outs occur over the Davis Strait where the sea ice remains. This is demonstrated very well by the July 2000 panel in Figure 4.5.

The Stokkseyri radar in Iceland is oriented such that it looks nearly perpendicular to the FOV of the Goose Bay radar across Greenland and the Davis Strait (Figure 4.6). Minor technical issues with operation of the radar in 2000 cause the color streaking seen in alternating beams. In all months except February and March, the western coastline of Greenland clearly defines the boundary of ground scatter occurrence nearest the radar. The southernmost extent of the Davis Strait within the Stokkseyri FOV which remains uncovered year-round is the most productive source of backscatter in all months except August and September.

We next consider the Saskatoon and Kapuskasing radars which look primarily over the Hudson Bay to the west of Baffin Island. During winter months when the Hudson Bay is covered by sea ice, the majority of backscatter observed by the Saskatoon radar comes from the land to the north of the Bay (Figure 4.7). This reverses in the summer months when the sea ice has melted and the sea surface within the Hudson Bay is much more productive of backscatter. It is interesting to note that in the month of June, the small bright patch of ground scatter occurrence seen at the mouth of the Hudson Bay aligns very well with a break in the sea ice cover.

Figure 4.8 shows results from the Kapuskasing radar as it looks directly north over the Hudson Bay at an angle to the Saskatoon radar FOV. In October 2000, the contours of ground scatter occurrence follow the northern coastline of the Hudson Bay very well suggesting strong backscatter from the sea surface in the Bay. There is little to no azimuthal variation in ground scatter seen during winter months (January–March) because the ice-covered Hudson Bay lies beneath nearly the entire backscatter region. During the summer months (June and July) when ionospheric conditions allow scattering from further ranges, bright patches of productive backscatter regions are aligned with sea surfaces where the Arctic ice has recently melted.

4.3.1 Goose Bay

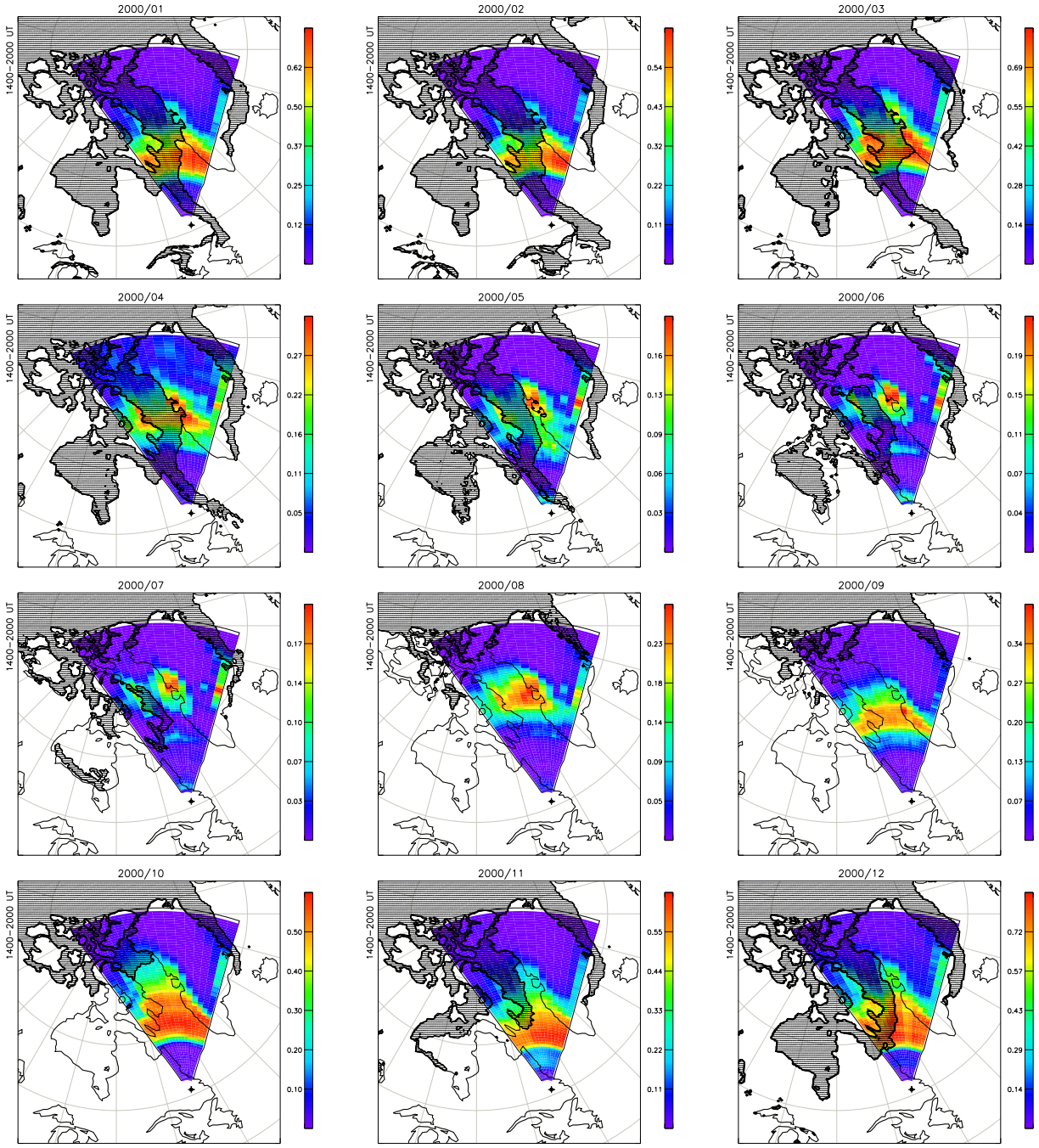

Figure 4.5: Monthly ground scatter occurrence rates for Goose Bay radar, averaged over 14:00-20:00 UT for the year 2000. Extent of sea ice cover at end of each month is denoted by shaded regions.

4.3.2 Stokkseyri

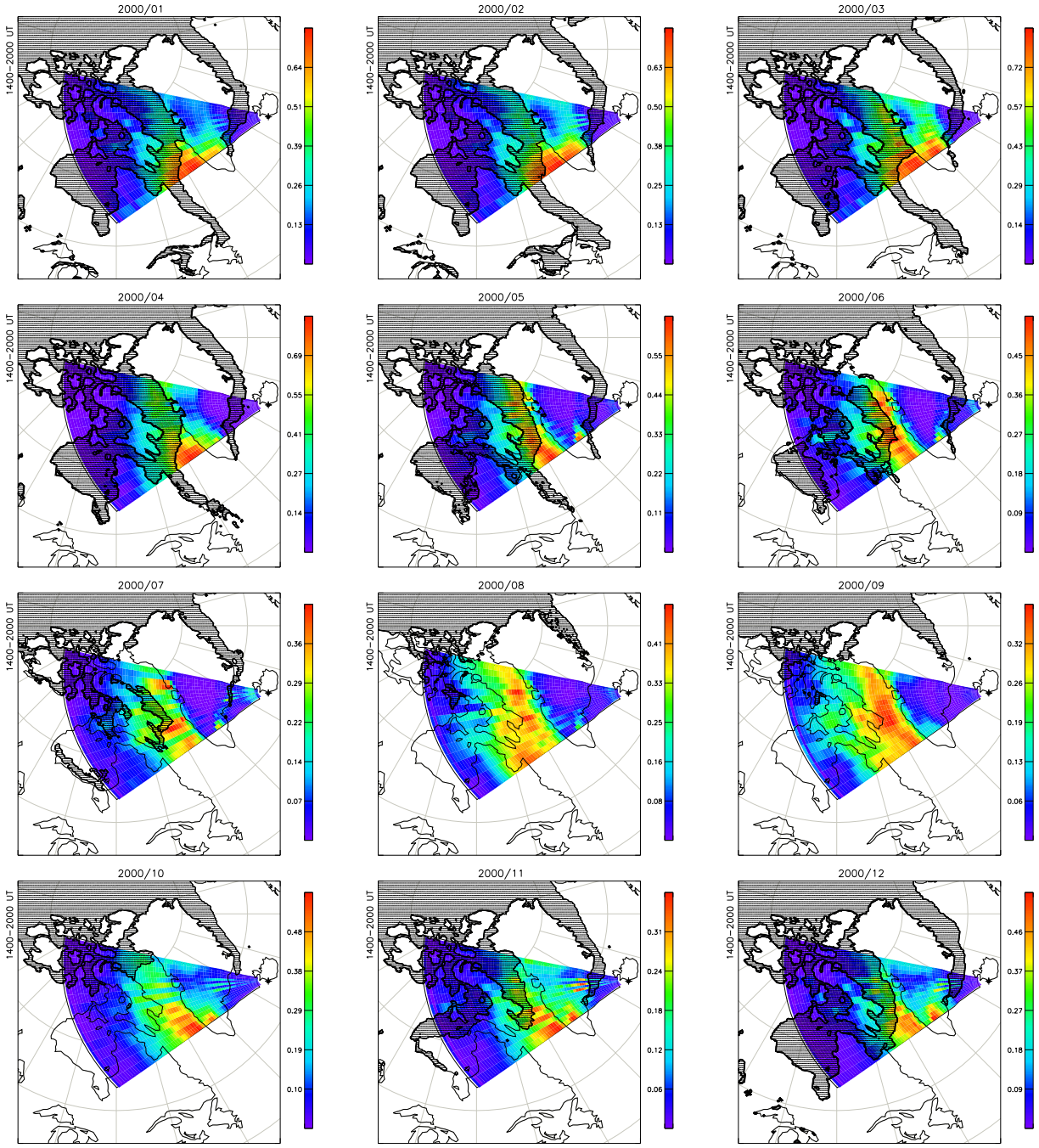

Figure 4.6: Monthly ground scatter occurrence rates for Stokkseyri radar, averaged over 14:00-20:00 UT for the year 2000. Extent of sea ice cover at end of each month is denoted by shaded regions.

4.3.3 Saskatoon

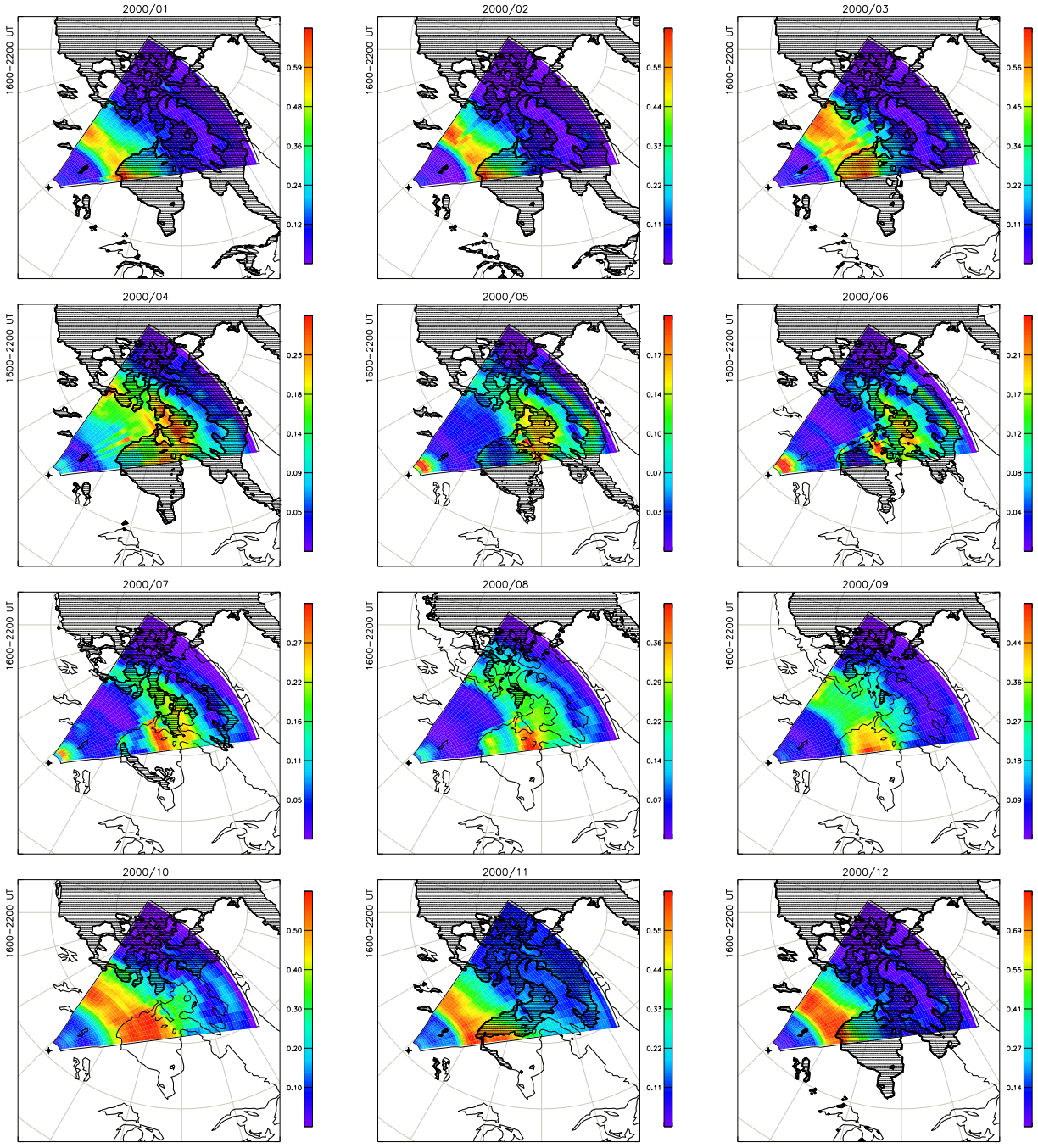

Figure 4.7: Monthly ground scatter occurrence rates for Saskatoon radar, averaged over 16:00-22:00 UT for the year 2000. Extent of sea ice cover at end of each month is denoted by shaded regions.

4.3.4 Kapuskasing

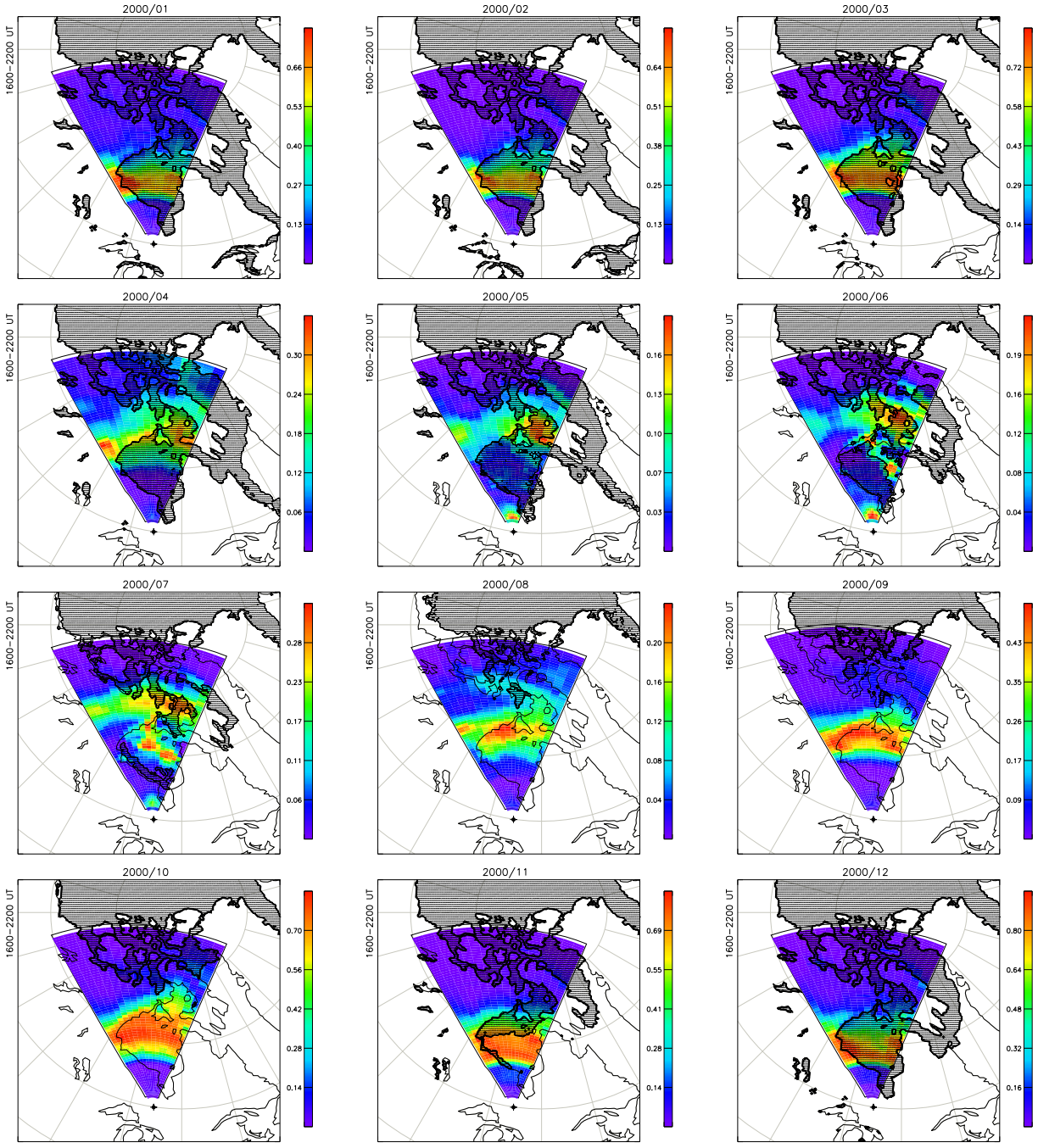

Figure 4.8: Monthly ground scatter occurrence rates for Kapuskasing radar, averaged over 16:00-22:00 UT for the year 2000. Extent of sea ice cover at end of each month is denoted by shaded regions.

4.4 Summary

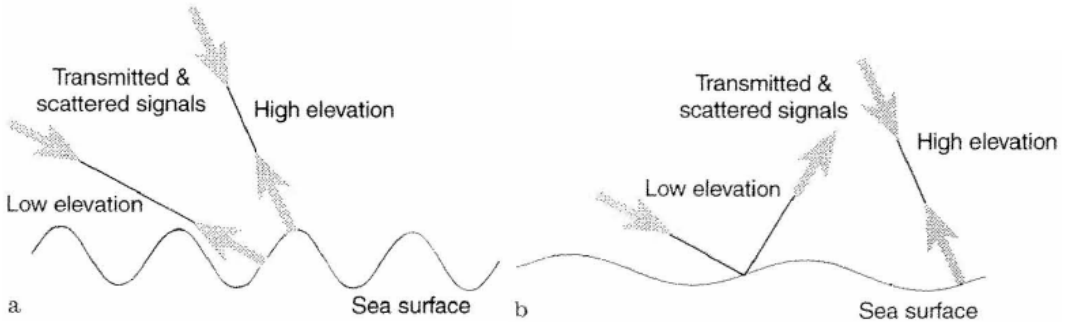

Figure 4.9: Sea surface scattering mechanism for (a) rough sea and (b) smooth sea [*Shand et al.*, 1998].

We have calculated ground scatter occurrence rates for four high-latitude SuperDARN radars and compared them to Arctic sea ice boundaries derived from satellite observations. Regions covered by sea ice are shown to be weak scatterers for the HF signals transmitted by SuperDARN radars. Sea surfaces not covered by ice are shown to produce more easily detectable backscatter than land regions in Canada and Greenland at comparable ranges. Expected scattering mechanisms from both rough and smooth sea surfaces can be seen in Figure 4.9; these scattering concepts are analogous to land features such as mountains and plains regions, respectively. The spatial accuracy of these ground satter results are influenced by several factors: seasonal ionospheric propagation conditions, relatively large range cell resolution (45 km), and the need for a thick daytime ionosphere to reflect radar signals down to the Earth's surface. Monthly statistics have been calculated to remove the influence of daily geomagnetic effects on propagation conditions. Operating modes could be scheduled to increase radar range resolution to 15 km to more easily detect surface scattering boundaries, although this would decrease the potential backscattered power within each range cell. Future work includes building a ground reflectivity model for predicting SuperDARN ground scatter over Arctic regions, as well as comparing backscatter from ocean

surfaces to satellite altimeter measurements of sea surface roughness.

Acknowledgments

The author acknowledges the National Snow and Ice Data Center, NOAA, for providing the online access to sea ice data. The author also thanks P. V. Ponomarenko for valuable discussions regarding previous work and providing guidance for accessing sea ice data. A portion of this work was presented as a final project for the ECE 6104 Microwave Remote Sensing of the Earth's Surface course instructed by Dr. Gary Brown.

Chapter 5

Conclusions/Future Work

The motivation for this research is to gain a better understanding of the relationship between large-scale plasma density structures and small-scale irregularities in the ionosphere using measurements from ground-based GPS receivers and SuperDARN HF radars. In Chapter 2, the method for calculating ionospheric total electron content (TEC) from the group delays of L1 and L2 GPS signals was introduced. Online plotting tools have been developed for direct comparison of globally gridded GPS TEC processed at MIT Haystack Observatory and SuperDARN observations. A localized region of enhanced TEC over the central United States was discovered after producing monthly maps of average TEC for geomagnetically quiet conditions. An automated search algorithm was developed in an attempt to characterize the frequency of occurrence of this phenomenon. The anomaly's solar cycle and local time dependence will continue to be investigated using a statistical approach. Future work may involve identifying receiver sites making line-of-sight TEC measurements through the anomaly region for a smaller-scale approach.

The relationship of convection electric fields to the formation of a polar tongue of ionization (TOI) from mid-latitude plumes of storm enhanced density (SED) was discussed in Chapter 3. Two cases of TOI formation from SED were presented for a geomagnetic storm on 26 September 2011. During the first period, plasma was transported from the dayside mid-latitude ionosphere and into the polar cap by enhanced convection electric fields extending to

middle latitudes. During the second interval the dayside convection electric fields retreated to higher latitudes, leaving behind a fossil SED feature elongating in magnetic local time as its base co-rotated with the Earth. The construction of new mid-latitude SuperDARN radars in the Azores and Aleutian Islands will allow for greater local time coverage of plasma transport at mid-latitudes during future SED/TOI events.

The ground surface effects on occurrence of radar backscatter was demonstrated for four high-latitude SuperDARN radars in Chapter 4. Monthly ground scatter occurrence rates were calculated for the Goose Bay, Stokkseyri, Saskatoon, and Kapuskasing radars using the criteria described by *Ponomarenko et al.* [2010]. By overlaying sea ice boundaries independently derived from satellite observations, it was shown that rough sea surfaces and coastlines are more productive of HF radar backscatter than regions covered in sea ice. Future work on this topic includes characterizing the reflectivity of sea ice to build a predictive model for seasonal ground surface effects on HF radar backscatter. This could be used to improve the accuracy of existing ray-tracing techniques which only consider ionospheric effects. HF backscatter properties from sea surfaces will also be compared to satellite altimeter measurements of sea surface roughness.

References

Anderson, P. C., R. A. Heelis, and W. B. Hanson (1991), The ionospheric signatures of rapid subauroral ion drifts, *J. Geophys. Res.*, *96*(A4), 5785–5792.

André, D., G. J. Sofko, K. Baker, and J. MacDougall (1998), SuperDARN interferometry: Meteor echoes and electron densities from groundscatter, *J. Geophys. Res.*, *103*(A4), 7003–7015.

Baker, J. B. H., R. A. Greenwald, J. M. Ruohoniemi, K. Oksavik, J. W. Gjerloev, L. J. Paxton, and M. R. Hairston (2007), Observations of ionospheric convection from the Wallops SuperDARN radar at middle latitudes, *J. Geophys. Res.*, *112*(A1), 1303.

Ballatore, P., J. P. Villain, N. Vilmer, and M. Pick (2001), The influence of the interplanetary medium on SuperDARN radar scattering occurrence, *Ann. Geophys.*, *18*, 1576–1583.

Basu, Su., S. Basu, J. J. Makela, E. MacKenzie, P. Doherty, J. W. Wright, F. Rich, M. J. Keskinen, R. E. Sheehan, and A. J. Coster (2008), Large magnetic storm-induced nighttime ionospheric flows at midlatitudes and their impacts on GPS-based navigation systems, *J. Geophys. Res.*, *113*(A3), A00A06.

Chisham, G., M. Lester, S. E. Milan, M. P. Freeman, W. A. Bristow, A. Grocott, K. A. McWilliams, J. M. Ruohoniemi, T. K. Yeoman, P. L. Dyson, et al. (2007), A decade of the Super Dual Auroral Radar Network (SuperDARN): Scientific achievements, new techniques and future directions, *Surv. Geophys.*, *28*(1), 33–109.

Clausen, L. B. N., et al. (2012), Large-scale observations of a subauroral polarization stream by midlatitude SuperDARN radars: Instantaneous longitudinal velocity variations, *J. Geophys. Res.*, *117*(A5), A05306.

Coster, A. J., J. C. Foster, P. J. Erickson, and F. J. Rich (2001), Regional GPS mapping of storm enhanced density during the 15-16 July 2000 geomagnetic storm, in *ION GPS 2001 Proceedings*, Salt Lake City, Utah, 2531–2539.

Coster, A. J., J. C. Foster, and P. J. Erickson (2003), Monitoring the ionosphere with GPS: Space weather, *GPS World*, *14*(5), 42–49.

Coster, A. J., M. Colerico, J. C. Foster, and J. M. Ruohoniemi (2006), Observations of the tongue of ionization with GPS TEC and SuperDARN, *Haystack Observatory, Westford, MA*.

Coster, A. J., M. J. Colerico, J. C. Foster, W. Rideout, and F. Rich (2007), Longitude sector comparisons of storm enhanced density, *Geophys. Res. Lett.*, *34*(18), L18,105.

Coster, A. J. (2011), A Student Tutorial: Using GPS to Study Magnetospheric-Ionospheric Coupling, *CEDAR-GEM Joint Workshop, Santa Fe, NM.*

Cowley, S. W. H., and M. Lockwood (1996), Time-dependent flows in the coupled solar wind-magnetosphere-ionosphere system, *Adv. Space Res.*, *18*(8), 141–150.

de Larquier, S., J. M. Ruohoniemi, J. B. H. Baker, N. Ravindran Varrier, and M. Lester (2011), First observations of the midlatitude evening anomaly using Super Dual Auroral Radar Network (SuperDARN) radars, *J. Geophys. Res.*, *116*, A10321.

Ecklund, W. L., B. B. Balsley, and R. A. Greenwald (1975), Crossed beam measurements of the diffuse radar aurora, *J. Geophys. Res.*, *80*(13), 1805–1809.

Evans, J. V., J. M. Holt, W. L. Oliver, and R. H. Wand (1983), The fossil theory of nighttime high latitude F region troughs, *J. Geophys. Res.*, *88*(A10), 7769–7782.

Fejer, B. G., and M. C. Kelley (1980), Ionospheric irregularities, *Rev. Geophys.*, *18*(2), 401–454.

Fetterer, F. and K. Webster (2011), IMS Daily Northern Hemisphere Snow and Ice Analysis at 4 km and 24 km Resolution, *National Snow and Ice Data Center, Boulder, CO.*

Foster, J. C. (1993), Storm time plasma transport at middle and high latitudes, *J. Geophys. Res.*, *98*(A2), 1675–1689.

Foster, J. C., M. J. Buonsanto, M. Mendillo, D. Nottingham, F. J. Rich, and W. Denig (1994), Coordinated stable red arc observations: Relationship to plasma convection, *J. Geophys. Res.*, *99*(A6), 11429–11439.

Foster, J. C., and W. J. Burke (2002), SAPS: A new categorization for sub-auroral electric fields, *EOS Trans. AGU*, *83*(36), 393.

Foster, J. C., and H. B. Vo (2002), Average characteristics and activity dependence of the subauroral polarization stream, *J. Geophys. Res.*, *107*(A12), 1475.

Foster, J. C., A. J. Coster, P. J. Erickson, F. J. Rich, and B. R. Sandel (2004), Stormtime observations of the flux of plasmaspheric ions to the dayside cusp/magnetopause, *Geophys. Res. Lett.*, *31*, L08809.

Foster, J. C., et al. (2005), Multiradar observations of the polar tongue of ionization, *J. Geophys. Res.*, *110*(A9), A09S31.

Getting, I. A. (1993), Perspective/navigation-the global positioning system, *IEEE Spectrum*, *30*(12), 37–38.

Greenwald, R. A., W. Weiss, E. Nielsen, and N. R. Thomson (1978), STARE: A new radar auroral backscatter experiment in northern Scandinavia, *J. Geophys. Res.*, *13*(6), 1021–1039.

Greenwald, R. A., K. B. Baker, and J. P. Villain (1983),Initial studies of small-scale F region irregularities at very high latitudes, *Radio Sci.*, *18*(6), 1122–1132.

Greenwald, R. A., K. B. Baker, R. A. Hutchins, and C. Hanuise (1985), An HF phased-array radar for studying small-scale structure in the high-latitude ionosphere, *Radio Sci.*, *20*(1), 63–79.

Greenwald, R. A., et al. (1995), DARN/SUPERDARN: A global view of the dynamics of high-latitude convection, *Space Sci. Rev.*, *71*(1), 761–796.

Greenwood, R. I., M. L. Parkinson, P. L. Dyson, and E. W. Schulz (2011), Dominant ocean wave direction measurements using the TIGER SuperDARN systems, *J. Atmos. Sol.-Terr. Phys.*, *73*(16), 2379–2385.

Grocott, A., S. E. Milan, J. B. H. Baker, M. P. Freeman, M. Lester, and T. K. Yeoman (2011), Dynamic subauroral ionospheric electric fields observed by the Falkland Islands radar during the course of a geomagnetic storm, *J. Geophys. Res.*, *116*(A11), A11,202.

Guier, W. H. and G. C. Weiffenbach (1993), A satellite Doppler navigation system, *Proceedings of the IRE*, *48*(4), 507–516.

Heppner, J. P., and N. C. Maynard (1987), Empirical high-latitude electric field models, *J. Geophys. Res.*, *92*(A5), 4467–4489.

Hosokawa, K., K. Shiokawa, Y. Otsuka, T. Ogawa, J.-P. St-Maurice, G. J. Sofko, and D. A. Andre (2009), Relationship between polar cap patches and field-aligned irregularities as observed with an all-sky airglow imager at Resolute Bay and the PolarDARN radar at Rankin Inlet, *J. Geophys. Res.*, *114*(A3), A03,306.

Hosokawa, K., T. Tsugawa, K. Shiokawa, Y. Otsuka, N. Nishitani, T. Ogawa, and M. R. Hairston (2010), Dynamic temporal evolution of polar cap tongue of ionization during magnetic storm, *J. Geophys. Res.*, *115*(A12), A12,333.

Hughes, W. J. (1995), The Magnetopause, Magnetotail, and Magnetic Reconnection, in *Introduction to Space Physics*, edited by M. G. Kivelson and C. T. Russell, pp. 227-287, Cambridge University Press, New York, New York.

Keskinen, M. J. and S. L. Ossakow (1983),Theories of high-latitude ionospheric irregularities: A review, *Radio Sci.*, *18*(6), 1077–1091.

King, J., and N. Papitashvili (2006), One min and 5-min solar wind data sets at the Eart's bow shock nose, *NASA Goddard Space Flight Cent., Greenbelt, MD.*

Kintner, P. M. (1999), *Global Positioning System Theory and Design*.

Knudsen, W. C. (1974), Magnetospheric convection and the high-latitude F2 ionosphere, *J. Geophys. Res.*, *79*(7), 1046–1055.

Kunduri, B. S. R., J. B. H. Baker, J. M. Ruohoniemi, L. B. N. Clausen, A. Grocott, E. G. Thomas, M. P. Freeman, and E. R. Talaat (2012), An examination of inter-hemispheric conjugacy in a subauroral polarization stream, *J. Geophys. Res.*, *117*(A8), A08,225.

Luhmann, J. G. (1995), Ionospheres, in *Introduction to Space Physics*, edited by M. G. Kivelson and C. T. Russell, pp. 183-202, Cambridge University Press, New York, New York.

Oksavik, K., R. A. Greenwald, J. M. Ruohoniemi, M. R. Hairston, L. J. Paxton, J. B. H. Baker, J. W. Gjerloev, and R. J. Barnes (2006), First observations of the temporal/spatial variation of the sub-auroral polarization stream from the SuperDARN Wallops HF radar, *Geophys. Res. Lett.*, *33*, L12,104.

Ponomarenko, P. V., J.-P. St. Maurice, G. C. Hussey, and A. V. Koustov (2010), HF ground scatter from the polar cap: Ionospheric propagation and ground surface effects, *J. Geophys. Res.*, *115*, A10310.

Rideout, W., and A. Coster (2006), Automated GPS processing for global total electron content data, *GPS Solutions*, *10*(3), 219–228.

Ruohoniemi, J. M., and R. A. Greenwald (1996), Statistical patterns of high-latitude convection obtained from Goose Bay HF radar observations, *J. Geophys. Res.*, *101*(A10), 21,743–21.

Ruohoniemi, J. M., and K. B. Baker (1998), Large-scale imaging of high-latitude convection with Super Dual Auroral Radar Network HF radar observations, *J. Geophys. Res.*, *103*(A9), 20,797–20.

Sato, T. (1959), Morphology of ionospheric F2 disturbances in the polar regions: A linkage between polar patches and plasmaspheric drainage plumes, *Rep. Ionos. Res. Space Res. Jpn.*, *13*, 91.

Sato, T., and G. F. Rourke (1964), F-region enhancements in the Antarctic, *J. Geophys. Res.*, *69*(21), 4591–4607.

Shand, B. A., S. E. Milan, T. K. Yeoman, P. J. Chapman, D. M. Wright, T. B. Jones, and L. T. Pederson (1998), CUTLASS HF radar observations of the Odden ice tongue, *Ann. Geophys.*, *16*, 280–282.

Shaw, M., K. Sandhoo, and D. Turner (2000), Modernization of the Global Positioning System, *DTIC Document*.

Shepherd, S. G., and J. M. Ruohoniemi (2000), Electrostatic potential patterns in the high-latitude ionosphere constrained by SuperDARN measurements, *J. Geophys. Res.*, *105*(A10), 23,005–23.

Tsunoda, R. T. (1988), High-latitude F region irregularities: A review and synthesis, *Rev. Geophys.*, *26*(4), 719–760.

Yionoulis, S. M. (1998), The Transit Satellite Geodesy Program, *Johns Hopkins APL Technical Digest*, *19*(1), 37.

Zhang, S. R., J. C. Foster, J. M. Holt, P. J. Erickson, and A. J. Coster (2012), Magnetic declination and zonal wind effects on longitudinal differences of ionospheric electron density at midlatitudes, *J. Geophys. Res.*, *117*, A08329.